Faculty of Physics
Sofia University "St. Kliment Ohridski"

Victor Ivaylov Danchev

Constraining strong regime gravity through analysis of compact astrophysical objects

SUMMARY

of a thesis for the award of the educational and scientific degree
"'DOCTOR"'

Professional direction 4.1 Physical sciences
Scientific speciality: 01.03.01 Theoretical and mathematical physics

Doctoral supervisor:
Prof. Stoytcho Yazadjiev

Scientific consultant:
Dr. Daniela Doneva,
Eberhard Karls University of Tübingen

Sofia • 2023

The doctoral student is enrolled in full-time doctoral studies at the Department of Theoretical Physics at the Faculty of Physics of SU "St. Kliment Ohridski". The thesis research was conducted at the Faculty of Physics of Sofia University.

The thesis consists of 144 pages divided into 7 chapters. It contains 27 figures and the bibliography covers 157 titles.

The thesis was discussed at a meeting of the departmental council in the Department of Theoretical Physics of the Faculty of Physics, SU "St. Kliment Ohridski", held on 18.01.2023, and referred for defense with scientific jury with members:

prof. Radoslav Hristov Rashkov (Faculty of Physics at SU "St. Kliment Ohridski")
prof. Emil Rafaelov Nissimov (IRNE BAS)
prof. Valentina Borissova Petkova (IRNE BAS)
prof. Svetlana Yordanova Pacheva (IRNE BAS)
prof. Vladimir Krastev Dobrev (IRNE BAS)

Contents

Motivation, purpose and problems of the thesis

Three different classes of alternative gravitational theories are reviewed in the dissertation, each of which is a promising candidate for extending the General Theory of Relativity, due to their self-consistency and good agreement with observations on cosmological and astrophysical scale. The purpose of the dissertation is to explore compact objects in these theories in order to constrain them in the strong regime of gravity through different modern observations.

A new class of compact objects have been explored, known as topological neutron stars. These objects exist in Tensor-Multi-Scalar Theories (TMST) of gravity. The properties of these objects have been explored for the first time under slow rotation and it has been shown that they obey two well-known universal relations (relating which do not depend on the equation of state) which can be used to differentiate not only the theory, but also the topological charge of these objects.

Several important observational characteristics in the electromagnetic spectrum were explored for different masses and spin rates of these compact objects: the innermost stable circular orbit (ISCO), orbital and epicyclic frequencies. New observational effects have been observed, based on the non-monotonic behaviour of the theory coupling function.

A new class of universal relations at the maximum mass point of a given solution branch for Scalar-Tensor Theory (STT) neutron stars were explored, which were only shown to hold in General Relativity prior to this study. It has been proven that STTs obey this novel type of universality and that the relations have different parameters based on the theory parameters, through the exploration of 53 Equations of State (EOS). It has been shown how EOS or theory parameters can be constrained based on the initial data, using known physical relations between matter properties and measured neutron star properties. This type of universality has been explored for the first time with the addition of non-baryonic EOS.

Strong constraints were placed on scalarization in scalar-Gauss-Bonnet (sGB) theories, using the changes in the orbital periods of three binary white dwarf – neutron star systems and 12 equations of state (EOS) through Bayesian analysis. The obtained theory parameter constraints have been translated to constraints on the maximum mass and topological charge of scalarized sGB black holes.

Structure and volume of the thesis

Chapter 1 – Introduction.

Chapter 2 briefly outlines General Relativity and the three alternative theories of gravity explored in this dissertation. The relevant field equations are obtained from the actions of the theories.

Chapter 3 derives the structure equations for static compact objects in General Relativity and outlines the general strategy to be followed when obtaining the analogous equations in other theories of gravity. It introduces the notion of slow rotation for compact objects and extends the structure equations to first order in angular velocity. It provides some background theory on the equation of state and its relevancy for compact objects as well as the most standard forms used for numerics. Furthermore, it defines important properties of the space-time around compact objects such as the Innermost Stable Circular Orbit (ISCO), orbital and epicyclic frequencies. It then provides a definition of two universal relations explored further in the work. Lastly, it provides a summary of the energy loss due to gravitational waves emission in close binaries and the orbital inspiral it leads to.

Chapter 4 outlines the primary numerical methods which were used by the author to obtain the various original results.

Chapters 5, 6 and 7 are dedicated to the author's original results.

Chapter 5 presents results for a novel class of compact objects called topological neutron stars in the context of Tensor-Multi-Scalar theories (TMSTs) of gravity. It begins with the theory formulation and derivation of the relevant structure equations for static and slowly rotating neutron stars in the theory. It then proceeds with the results presentation, broken into 2 parts. The first part shows that well-known universal relations from GR and STTs theories hold also for topological neutron stars and that they can provide a distinction between both the theories and the topological charge of these neutron stars in TMSTs independently of the equation of state. The second part outlines the results for ISCO, orbital and epicyclic frequencies around topological neutron stars and comments on the possibility to distinguish such objects based on qualitative and quantitative differences in accretion disks and X-ray spectra. All results and their implications are commented upon.

Chapter 6 presents the results for a novel class of universal relations between physical quantities of neutron stars applied at the maximum-mass point of sequences of compact objects. These had previously only been explored and shown to hold true in General Relativity but were proven to be valid also for Scalar-Tensor theories (STTs). It is shown that they can be used to provide EOS-independent means of differentiating between theory parameters or, if the theory is fixed, to provide a means of constraining different nuclear equations of state. All results and their implications are commented upon.

Chapter 7 presents the results for constraining Gauss-Bonnet theories of gravity through direct Bayesian analysis applied in comparison with observed neutron star – white dwarf systems with very precisely measured orbital decay rates. It begins with the theory formulation and derivation of the structure equations for the compact objects. It proceeds with the definition of the likelihood function to be used in the Bayesian analysis and discussion of its applicability to obtain objective constraints on alternative theories. It then proceeds to outline the results which are in the form of posterior distributions for the allowed parameters of the theory based on observations. These are performed for two different coupling functions and are then translated to limitations on the maximum allowed black hole mass and scalar charge for one of these functions which does not require spin-induced scalarization of the black holes.

1 Introduction

The inherent non-linearity of gravitational theories makes analytical progress very difficult, if at all possible. There are well known perturbation methods in the weak-field regime which provide precise description on the scale of the Solar System for example, but any such method breaks down in the strong regime. Very few exact solutions are known and these are typically for vacuum solutions (in the absence of sources) or for idealised mass-energy distributions. While these are useful for general intuition as "toy models" and may have good applicability in certain situations, the realistic solutions for the structure of space-time on the scale of the Universe or around compact objects are almost exclusively treated numerically.

Compact objects are of prime interest for different branches of physics as they are natural laboratories for high–energy phenomena from multiple realms. Treating their internal structure analytically is not possible unless severe approximations are made. The internal pressure of such objects is so high that the density can reach (and even exceed) that of atomic nuclei. Since there are no direct experiments available which can provide measurements into such high-density matter, modelling the internal structure of such objects is critical for increasing our understanding of the domain.

The discovery of the Universe's accelerated expansion in the late 20^{th} century is a prime experimental motivation to consider alternative theories of gravity to General Relativity. While a solution can be included in GR, it requires additional exotic sources of energy (collectively dark energy) which have negative energy density. Most alternative theories of gravity provide

such sources naturally as well as mechanisms for producing the same effects as negative energy density in a more physically-founded manner. Furthermore, theoretical attempts to unify gravity with the rest of the forces in Nature have shown that either Quantum Field Theory (QFT) or General Relativity (most likely both) are incomplete. In either case, GR cannot be renormalized in the same way as other theories and one of the reasons for modifying it is to make it renormalizable. Most realistic alterantive theories to GR, however, do not predict any measurable differences from it on the scale of the Solar System, which makes the exploration of strong regime gravity so important. Different theories of gravity lead to different structure and physical properties of compact objects such as neutron stars. The mass, radius, moment of inertia and the structure of space-time outside of such an object will depend on the theory and so these observational traits can be used to refine our understanding of gravity and lead us towards GR's potential successor.

Optical sensors are not very effective for measuring any of these properties due to the very small dimensions of compact objects and their generally low emissions in this range. Historically (and today), the most precise observations of neutron stars and in particular the class of pulsars has come from radio or X-ray observatories. Gravitational waves recently became an important tool for astrophysics but they are only measurable in the final stages of orbital inspiral events soon before compact objects merge. These have already provided several insights on the structure of matter and are of primal importance for the continued refinement of the nuclear equation of state knowledge. Given the frequency of such events for compact objects, however, for the conceivable future X-ray and radio will likely not lose their niche. The reason for their usefulness is that most compact objects have strong magnetic field and high spin rates, leading to a wide range of electromagnetic phenomena when accreting matter from other nearby objects. The spectrum of such an accretion disc is directly related to the object's properties. In the case of pulsars, the very precise pulse period due to the object's rotation allows for a wide array of properties and orbital parameters to be measured with very high precision when in binary. Nevertheless, the exploration of these objects and its implications for gravity and high energy physics is a joint effort between theory, numerical models and observations from all of these sources. What is referred to as multi-messenger astronomy (simultaneous observations from gravitational and electromagnetic waves as well as any cosmic rays from the same event) will become even more important with the growing sensitivity of our sensors.

2 Gravitational Theories

The first mathematically formulated Theory of Universal Gravitation (and indeed formal concept of gravity) came about in 1687 and was essentially unchallenged for 200 years, shifting the paradigm in Physics for many reasons. The concept of Newtonian Gravity was so deeply embedded into the thinking of 19th century physicists, that it took nearly half a century of hunting for intermercurial planets [1] until its fidelity was seriously put under debate. In that case, the deviation from Newtonian gravity was so miniscule – a difference of just 38 arcseconds per century in the perihelion advance of Mercury as measured by Le Verriere (later refined to 43" by Newcomb) [1].

It was only in 1915 when Hilbert, Grossman and Einstein formulated a new theory of gravity - the General Theory of Relativity, a decade after the triumph of the Special Theory of Relativity over Newtonian dynamics. While this extension did not change our views of the Solar System appreciably (except for some niche applications such as GNSS satellites), it brought about a new revolution, turning the centuries old concept of a force into geometrical curvature and completely redefining the meaning of gravity. General Relativity (GR) is the currently accepted theory of gravity and it is verified to an amazing precision on the scale of the Solar System, however, it is far from unchallenged today. Many motivations exist for

GR's modification due to observations on the Cosmological scale as well as various theoretical arguments.

Some of the most promising extensions of General Relativity (GR) are based on additional fields which contribute to Gravity both as additional sources through their energy-momentum tensor and through some direct coupling to the metric. Most of these rely on some scalar, vector or tensor fields which carry their own matter actions but also couple the gravitational action to effectively add more channels of non-linearity in the theory, while preserving the overall idea of a metric theory and the core concept of space-time. Other, more exotic theories are completely non-metric and introduce torsion in the manifold. In all cases, a viable alternative theory of gravity must agree with General Relativity in the weak-field regime at least to the accuracy of existing observations in order to be seriously considered. Like with Mercury's perihelion, however, we can expect that significant differences will arise specifically in the strong field regime, which makes compact objects such interesting laboratories for gravitational exploration.

2.1 General Relativity

General Relativity is a geometrical theory and the Einstein-Hilbert action which generates its field equations in vacuum is, naturally, the simplest geometrical invariant one can expect to form on a manifold - the Ricci scalar. All matter sources of gravity are generated simply by the actions of the fields which comprise that matter, giving a complete action for the theory as

$$S_{\mathrm{GR}} = \frac{c^4}{16\pi G}\int d^4x\sqrt{-g}R + S_{\mathrm{m}}(g_{\mu\nu}, \Psi_{\mathrm{m}}), \tag{1}$$

where R is the Ricci Scalar, g is the determinant of the metric tensor with components $g_{\mu\nu}$ of the manifold that is associated with space-time, G is the Newtonian gravitational constant and S_{m} is the combined action of all matter fields generating energy and momentum, collectively denoted as Ψ_{m}. Variation of (1) by the metric tensor is straightforward and leads to the Einstein field equations

$$R_{\mu\nu} - \frac{1}{2}Rg_{\mu\nu} = \frac{8\pi G}{c^4}T_{\mu\nu}, \tag{2}$$

where $T_{\mu\nu}$ is the energy-momentum tensor, defined by the functional derivative

$$T_{\mu\nu} = -\frac{2}{\sqrt{-g}}\frac{\delta S_{\mathrm{m}}}{\delta g_{\mu\nu}}. \tag{3}$$

While this tensor defines the matter sources of gravity, the structure of (2) carries significant non-linearity and gives rise to non-trivial dynamics even without sources.

Perhaps even more fundamental than the field equations is the divergence of the energy-momentum tensor

$$\nabla_\mu T^{\mu\nu} = 0, \tag{4}$$

which is usually referred to as "energy-momentum conservation". Equation (4) follows from the contracted Bianchi identities and the field equations, and carries within it the fundamental equalities of how matter interacts with space-time.

Equation (2) can be rewritten in a form which minimizes the number of explicit derivatives of the metric on the left-hand side. Taking a trace of both sides and defining $T^\mu_\mu = T$, one obtains the equivalent equation

$$R_{\mu\nu} = \frac{8\pi G}{c^4}\left(T_{\mu\nu} - \frac{1}{2}g_{\mu\nu}T\right), \tag{5}$$

which simplifies the process of finding compact objects structure equations.

For the most part of the dissertation, natural units have been assumed: $c = \hbar = 1$ for simplicity of the notation.

2.2 Scalar-Tensor theories of gravity

Two classes of scalar-tensor theories of gravity have been used in the dissertation, diferring by the number of scalar fields and the space of their outputs.

The first class are Tensor-Multi-Scalar Theories (TMST) of gravity, which are mathematically self-consistent and fit all known observations [2, 3]. TMSTs are characterized by a gravitational interaction mediated by the spacetime metric $g_{\mu\nu}$ and N scalar fields φ^a with values in a coordinate patch of an N-dimensional Riemannian manifold $\mathbb{E}^N$ (called target manifold) with a positive-definite metric $\gamma_{ab}(\varphi)$ on it. The Einstein frame action of the theory class we explore is given by

$$S = \frac{1}{16\pi G_*}\int d^4x\sqrt{-g}[R - 2g^{\mu\nu}\gamma_{ab}\nabla_\mu\varphi^a\nabla_\nu\varphi^b - 4V(\varphi)] + S_{\rm m}(A^2(\varphi)g_{\mu\nu}, \Psi_{\rm m}), \tag{6}$$

where G_* is the bare gravitational constant, R and ∇_μ are the Ricci scalar and the covariant derivative with respect to the Einstein frame metric $g_{\mu\nu}$, and $V(\varphi) \geq 0$ is the potential which is a function of all scalar fields. The conformal factor $A^2(\varphi)$, the target space metric γ_{ab} and the scalar fields potential $V(\varphi)$ specify the exact TMST.

The variation of (6) with respect to the Einstein frame metric components and the scalar fields gives the field equations of the theory in the Einstein frame as follows

$$R_{\mu\nu} = 8\pi G_*\left(T_{\mu\nu} - \frac{1}{2}Tg_{\mu\nu}\right) + 2\gamma_{ab}(\varphi)\nabla_\mu\varphi^a\nabla_\nu\varphi^b + 2V(\varphi)g_{\mu\nu}, \tag{7}$$

$$\nabla_\mu\nabla^\mu\varphi^a = -\gamma^a_{bc}(\varphi)g^{\mu\nu}\nabla_\mu\varphi^b\nabla_\nu\varphi^c + \gamma^{ab}(\varphi)\frac{\partial V(\varphi)}{\partial\varphi^b} - 4\pi G_*\gamma^{ab}(\varphi)\frac{\partial \ln A(\varphi)}{\partial\varphi^b}T, \tag{8}$$

where $T_{\mu\nu}$ is the Einstein frame energy-momentum tensor of the matter and $\gamma^a_{bc}(\varphi)$ are the Christoffel symbols with respect to the target space metric γ_{ab}, following closely the notation in [4].

The conservation law for the energy-momentum tensor takes the form

$$\nabla_\mu T^{\mu\nu} = \frac{\partial \ln A(\varphi)}{\partial\varphi^a}T\nabla^\nu\varphi^a, \tag{9}$$

summing over all scalar fields $a = 1, 2, ...N$.

It is standard when working with compact objects, to use the Einstein-frame quantiites for actually solving the equations but transform everything to the physical (Jordan) frame in the end since it describes the actual physical quantities. The relation between the two systems is the conformal factor which gives $\tilde{g}_{\mu\nu} = A^2(\varphi)g_{\mu\nu}$, where the physical frame quantities (Jordan frame) are denoted with tilde. It is easy to show that the relation between the EM tensor in the two frames is given by the inverse dependence $T_{\mu\nu} = A^2(\varphi)\tilde{T}_{\mu\nu}$. The pressure, density and 4-velocity are connected by the transformations $\rho = A^4(\varphi)\tilde{\rho}$, $P = A^4(\varphi)\tilde{P}$ and $u_\mu = A^{-1}(\varphi)\tilde{u}_\mu$ which follow directly from the ideal fluid energy-momentum tensor definition.

The second class are classical scalar-tensor theories (STTs), given by the Einstein-frame metric

$$S = \frac{1}{16\pi G_*}\int d^4x\sqrt{-g}(R - 2g^{\mu\nu}\partial_\mu\varphi\partial_\nu\varphi - V(\varphi)) + S_{\rm m}(A^2(\varphi)g_{\mu\nu}, \Psi_{\rm m}), \tag{10}$$

which is a subclass of (10) for a single field φ, which takes its values on the space-time $\varphi = \varphi(t, \vec{x})$. This class of theories is defined only by the functional dependence of the conformal factor $A^2(\varphi)$ and the potential $V(\varphi)$.

The field equations obtained from the variation of (10) are

$$R_{\mu\nu} = 8\pi G_* \left(T_{\mu\nu} - \frac{1}{2} T g_{\mu\nu} \right) + 2\nabla_\mu\varphi\nabla_\nu\varphi + \frac{1}{2} V(\varphi) g_{\mu\nu}. \tag{11}$$

$$\nabla_\mu\nabla^\mu\varphi = -4\pi G_* T \frac{d\ln A(\varphi)}{d\varphi} + \frac{1}{4}\frac{dV(\varphi)}{d\varphi}, \tag{12}$$

which are analogous to (7) and (8). Using the Bianchi identity and the field equations leads to the 4-divergence of the energy-momentum tensor in a form similar to (9), but with no summation over the field index

$$\nabla_\mu T^{\mu\nu} = \frac{d\ln A(\varphi)}{d\varphi} T \nabla^\nu\varphi. \tag{13}$$

2.3 Gauss-Bonnet theories of gravity

A class of alternative theories of gravity where scalarization was discovered a few years ago are the Gauss-Bonnet (GB) theories [5]. They are perhaps the most prominent subclass of quadratic theories of gravity defined by the addition of all possible geometrical invariants of second-order to the theory action in addition to the classical Einstein-Hilbert term [6]. A strong motivation behind these types of modifications of Einstein's theory comes from the attempts to quantize gravity.

Within the dissertation, a class of scalar Gauss-Bonnet (sGB) theories has been used, with the action

$$S = \frac{1}{16\pi G_*} \int d^4x\sqrt{-g} \left[R - 2\nabla_\mu\varphi\nabla^\mu\varphi + \lambda^2 f(\varphi)\mathcal{R}^2_{GB} \right] + S_{\rm m}(g_{\mu\nu}, \Psi_{\rm m}), \tag{14}$$

where R is the Ricci scalar and ∇_μ is the covariant derivative, both with respect to the spacetime metric $g_{\mu\nu}$. Lastly, the Gauss-Bonnet invariant is defined as $\mathcal{R}^2_{GB} = R^2 - 4R_{\mu\nu}R^{\mu\nu} + R_{\mu\nu\alpha\beta}R^{\mu\nu\alpha\beta}$ with respect to the spacetime Ricci and Riemann tensors. The resulting field equations from (14) are

$$R_{\mu\nu} = 8\pi G_* \left(T_{\mu\nu} - \frac{1}{2} T g_{\mu\nu} \right) - \left(\Gamma_{\mu\nu} - \frac{1}{2}\Gamma g_{\mu\nu} \right) + 2\nabla_\mu\varphi\nabla_\nu\varphi \tag{15}$$

$$\nabla_\alpha\nabla^\alpha\varphi = -\frac{\lambda^2}{4}\frac{df(\varphi)}{d\varphi}\mathcal{R}^2_{GB}, \tag{16}$$

where $T_{\mu\nu}$ is the matter energy-momentum tensor while $\Gamma_{\mu\nu}$ is defined as

$$\begin{aligned} \Gamma_{\mu\nu} = \quad & -R(\nabla_\mu\Psi_\nu + \nabla_\nu\Psi_\mu) - 4\nabla^\alpha\Psi_\alpha \left(R_{\mu\nu} - \tfrac{1}{2} R g_{\mu\nu} \right) + \\ & 4R_{\mu\alpha}\nabla^\alpha\Psi_\nu + 4R_{\nu\alpha}\nabla^\alpha\Psi_\mu - 4g_{\mu\nu}R^{\alpha\beta}\nabla_\alpha\Psi_\beta + 4R^\beta_{\mu\alpha\nu}\nabla^\alpha\Psi_\beta, \end{aligned} \tag{17}$$

and we have defined the auxiliary functions $\Gamma = \Gamma^\mu_\mu$ and

$$\Psi_\mu = \lambda^2 \frac{df(\varphi)}{d\varphi}\nabla_\mu\varphi. \tag{18}$$

By applying the field equations to the contracted Bianchi identities, one can show that the matter energy-momentum tensor satisfies a conservation law in the same form as that of GR

$$\nabla_\mu T^{\mu\nu} = 0. \tag{19}$$

3 Structure and properties of compact astrophysical objects

3.1 Compact objects

Compact objects are the final remains of main sequence stars after they have depleted all of their nuclear fuel. Depending on the original mass of a star, it will eventually end its life in one of three stages (or their more exotic counterparts): white dwarf, neutron star or black hole. As the name suggests, these objects are a lot more compact than classical stars, that is – they have a much smaller radius for the same mass. These objects maintain their internal pressure against gravity not through any kind of emission or nuclear reactions, but due to degenerate gas pressure predicted by Pauli's exclusion principle [7]. White dwarfs, for example, counteract their self-gravitation through the degenerate pressure of electrons, while neutron stars have a similar mechanism through degenerate pressure dominated by neutrons. This is also the reason for the much higher compactness of neutron stars, since the maximum degeneracy pressure which such a gas can support is proportional to its mass.

Given the extreme density and pressure in neutron stars, it is expected that other more exotic states of matter can also exist in their interior but after a certain maximum mass, a compact object's gravity is expected to overcome all degenerate gas pressure and other mechanisms and for that object to collapse into a black hole.

The characteristic which defines the gravity around a body to first order is the second power of its classical escape velocity as compared to the speed of light given by

$$\epsilon = \left(\frac{v_e}{c}\right)^2 = \frac{2MG}{c^2 R}, \tag{20}$$

where M is the object's mass, R is the object's radius and c is the speed of light. The parameter (20) is used as a characteristic dimensionless gravitational scale for different theories when treating them perturbatively in the so called post-Newtonian expansion.

Typical stellar objects such as planets and main sequence stars have ϵ on the order of 10^{-9} to 10^{-5} on their surfaces which shows the small relevance of relativistic corrections in their dynamics. For white dwarfs, $R \cong 5000$ km and $M \cong 1 - 1.4\ M_\odot$, leading to $\epsilon \cong 4 \times 10^{-4}$. The typical neutron star radius and mass, however, are on the order $R \cong 10 - 15$ km and $M \cong 1.4 - 2.2\ M_\odot$, leading to ϵ on the order of 0.14 to 0.33, which can no longer be neglected even to second or third order for meaningful dynamics! Unlike white dwarfs and neutron stars, black holes are not considered to have any physically meaningful solid surface. They are defined by a geometrical boundary called event horizon which is in fact defined (for a static black hole) by $\epsilon = 1$ in (20), which defines the geometrical surface of their event horizon (known as Schwarzschild radius for static black holes) as

$$R_s = \frac{2MG}{c^2}. \tag{21}$$

This radius is not a hard surface like for the remaining objects discussed, but the geometrical surface beyond which any information is causally impossible to exit "to the outside world". In more formal terms, any timelike or lightlike trajectories starting inside the event horizon will always remain within it. When speaking about the "radius of a black hole", one always means its event horizon (or in the case of rotating black holes, perhaps its ergosphere). Black hole masses can range from a few solar masses (for stellar black holes) to many millions of solar masses (for black holes found in galactic nuclei).

3.2 Equation of State

Matter inside compact objects can reach incredibly high density - as high as (or even higher than) that in nuclei. The nuclear saturation density is on the order of 2.5×10^{17} kg/m^3 (2.5×10^{14} g/cm^3), which is the scale to be considered for describing matter in the interior of neutron stars. At this scale, classical matter description is no longer applicable and quantum effects dominate. In practice, these effects are averaged from the microscopic theory and lead to dependencies between key macroscopic properties of the matter. Given the high density in compact objects, in practice one always assumes perfect fluid which is defined by its local isotropy. Such matter is effectively described only by its pressure P and density ρ. It can be shown that the energy-momentum tensor for such matter takes the form

$$T^{\mu\nu} = (P + \rho)u^\mu u^\nu + Pg^{\mu\nu}, \tag{22}$$

where ρ is in natural units ($c = 1$).

The relation between them $P = P(\rho)$ is referred to as Equation of State (EOS). This relation is obtained from the microscopic theory of the different constituent particles which contribute to the matter description, and it is required to solve the compact objects' structure equations. Describing matter with density higher than the nuclear saturation is a difficult problem due to the lack of direct measurements for the properties of such matter on Earth. There are some experiments which attempt to replicate the behaviour through collisions of heavy nuclei in order to form extremely high densities for short periods of time. Even in those experiments, however, one does not get the full picture since the ratio between protons and neutrons in nuclei is not the same as that in a neutron star. When solving the structure equations, therefore, one relies on theoretical models of high-density, high-energy nuclear matter. This is an important motivation for seeking universal relations such as those explored in the dissertation. Such relations, obtained from the physical quantities of the compact objects, are independent of the Equation of State (EOS) to a very high accuracy and allow for the gravitational theory to be constrained regardless of it. In a similar manner, given an assumption for the gravitational theory, numerical models of the compact objects and their observations contribute to the development of the nuclear interaction models at high densities.

Deriving equations of state is typically performed through classical and quantum statistical physical models relying on effective nuclear forces potentials in power expansions of the grand canonical ensemble. Most models start with baryon-only constituents which are experimentally well constrained from nuclear experiments (and expected closer to the crust of a neutron star), and some additional contributions of non-baryonic matter in the central regions. There can be multiple phases inside a neutron star beyond the crust and outer core, including color superconductive regions, neutron superfluid, vortex quasiparticles and possibly exotic states of matter such as quark matter or quark-gluon plasma. A typical methodology adopted by most is to parametrize each such model as a simple polytropic equation of state – an analytical form described by a power function which can be fitted to the numerical results for the given EOS obtained from the nuclear theory.

It has been shown that virtually all realistic EOS for certain constituents can be fitted to within a few % to such a description [8] using N separate polytropes

$$P(\rho) = K_i \rho^{\gamma_i}, \tag{23}$$

for $i = 1, 2, ...N$. Given such an anzatz, all remaining variables can be easily derived from the first law of thermodynamics, which when reparametrized in terms of the particle number

density lead to the form

$$P = K_i n_0 m_b \left(\frac{n}{n_0}\right)^{\gamma_i} \tag{24}$$

$$\rho = m_b n + \frac{P}{\gamma_i - 1}, \tag{25}$$

where n_0 is a reference particle density and m_b is a reference baryon mass. Given the multiple polytropes description, one can define a standard Maxwell construction for a first order phase transition between the different phases. This is a useful description as it can provide very good approximation to the actual nuclear EOS in analytical form and allows for direct constraints on a relatively small number of parameters K_i and γ_i ($2N$ in total based on the regions considered).

The difference between the physical properties of compact objects depending on the assumed equation of state can be seen on Fig. 1, which shows the relation between the mass and radius of static neutron stars in General Relativity (GR) for 10 different EOS which are among those used in the dissertation.

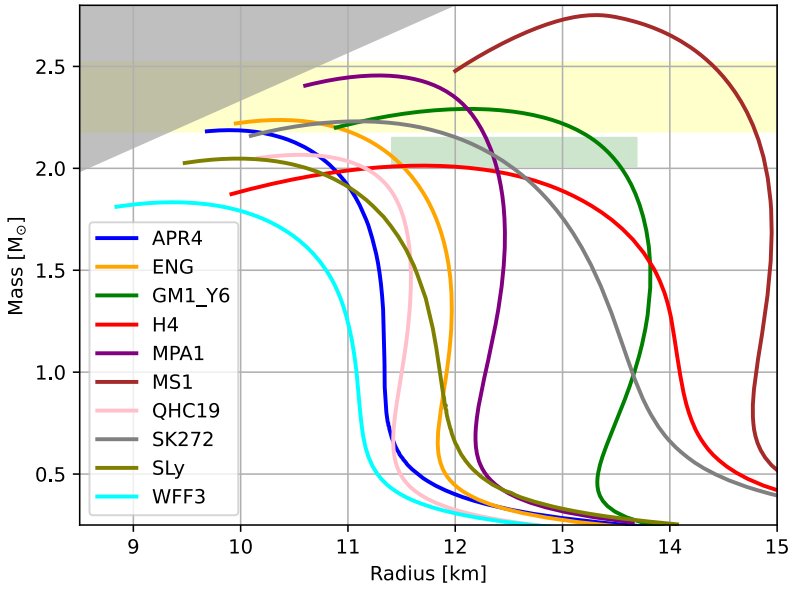

Figure 1: Comparison of the Mass-Radius relations for 10 different equations of state described in the legend which are some of the EOS used throughout this work. The gray area in the top left corner shows the causality breaking limit, the yellow and green zones show the measured mass and radius constraints for the two most massive neutron stars known to date PSR J0740+6620 and PSR J0952-0607 respectively.

As it can be seen, if mass and radius could be simultaneously measured, one could provide a very firm constraint, but due to the small radii of these objects, we must use different methods outlined in the following sections to deal with this uncertainty. The author has made use of both tabulated EOS and their polytropic approximations. All original results use multiple equations of state in order to explore the dependence on this unknown parameter and where possible, to confirm the independence of the results from the EOS.

3.3 Structure equations

Astrophysical objects have symmetries which reduce the complexity of the field equations (5) and their generalizations for alternative theories of gravity. While a general space-time metric

has 10 independent components, in practice, one uses an anzatz of the metric dictated by these space-time symmerties and obtains a smaller number of equations – the so called dimensionally reduced equations which must be solved to obtain the structure of compact objects. These reduced equations depend on the exact theory of gravity but the strategy for their finding is similar across all metric theories. The structure equations have been derived for three alternative theories of gravity which are explored in the dissertation in the respective chapters dealing with their results.

3.3.1 Static case

Taking all possible invariants in a static space-time with spherical symmetry produces a unique form of the metric, given by the line element

$$dS^2 = -e^{2\Gamma}dt^2 + e^{2\Lambda}dr^2 + r^2(d\theta^2 + \sin^2\theta d\varphi^2), \tag{26}$$

where $\Gamma(r)$, $\Lambda(r)$ are two functions which depend on the radial coordinate only. Given the form of the energy-momentum tensor defined by (22), both the left and right hand side of (5) are diagonal and it turns out that only 2 of the 4 equations are independent, giving us

$$\frac{1}{r^2}\frac{d}{dr}(r(1-e^{-2\Lambda})) = 8\pi G\rho \tag{27}$$

$$\frac{2}{r}e^{-2\Lambda}\frac{d\Gamma}{dr} - \frac{1}{r^2}(1-e^{-2\Lambda}) = 8\pi GP. \tag{28}$$

One can define an axiluary mass function $m(r)$ given by

$$e^{-2\Lambda} \equiv 1 - \frac{2Gm(r)}{r}. \tag{29}$$

The rationale behind this definition is the integration of (27) which naturally brings it about with the correspondence

$$m(r) = \int_0^r 4\pi r'^2\rho(r')dr'. \tag{30}$$

The obvious Newtonian interpretation of this mass function is that it holds the total mass enclosed by some radius r as one moves radially outward from the compact object. The GR interpretation is the same, keeping in mind that it is defined by some coordinate radius, which turns out to correspond to the standard spherical radial coordinate of Minkowski space-time in the asymptotics. This mass function is a constant outside of the compact object and allows us to find its mass as

$$M = \frac{R_s}{2G}(1-e^{-2\Lambda(R_s)}), \tag{31}$$

where the surface radius R_s is defined by $P(R_s) \equiv 0$.

One can show that for an alternative theory of gravity, the asymptotics of (30) once again define the mass of the compact object

$$\lim_{r\to\infty} e^{-2\Lambda} = 1 - \frac{2GM}{r}. \tag{32}$$

but unlike GR, the equality does not hold on the surface due to the additional sources arising from the extra fields and non-linear terms, so it should be interpreted as asymptotic equality.

One further equation can be obtained by using the divergence of the EM tensor (4), which results into the hydrostatic equilibrium condition for the compact object

$$\frac{dP}{dr} = -(P+\rho)\frac{d\Gamma}{dr}. \tag{33}$$

Using (33) and the definition (29), one can rewrite (27) and (28) into the more well-known form in GR

$$\frac{dP}{dr} = -\frac{G}{r^2}\frac{(P+\rho)(m+4\pi r^3 P)}{\left(1-\frac{2Gm}{r}\right)} \tag{34}$$

$$\frac{dm}{dr} = 4\pi r^2 \rho. \tag{35}$$

The equations (34) and (35) in this form are known as Tolman-Oppenheimer-Volkov (TOV) equations [9]. They have three unknown functions $P(r)$, $\rho(r)$ and $m(r)$ and so they must be augmented by one additional differential or algebraic equation. This is where the Equation of State (EOS) comes in - it provides a description of the dependence $P = P(\rho)$ from microscopic principles and allows for the system to be readily integrated numerically.

When working in alternative gravitational theories, one typically works directly in terms of Γ and Λ since the auxiluary function $m(r)$ does not have a direct interpretation except in the asymptotics. The strategy for obtaining the dimensionally reduced field equations in alternative theories of gravity is quite similar. For static solutions one uses the same metric anzatz (26) which produces 2 independent equations from the field equations ((11),(7) or (15) in our case). In cases with N additional fields such as all the theories considered in the dissertation, there are N additional independent field equation for each of the fields produced from the respective action variation. Lastly, one needs to take into account the equilibrium condition derived from the energy-momentum tensor divergence. Given the above, one has a total of 3 + N independent equations for 4 + N total unknown functions: $\Lambda(r)$, $\Gamma(r)$, $P(r)$, $\rho(r)$ and the N extra fields. As with General Relativity – the way to solve the system is to introduce a connection between pressure and density through the Equation of State (EOS). The specifics of each of the considered alternative gravitational theories are treated in the corresponding chapter with the results.

3.3.2 Slowly rotating case

Compact astrophysical objects are typically rotating with very high angular rates as compared to planets or main sequence stars. This fact is a simple consequence of the conservation of angular momentum during the original star's collapse, which leads to a large increase of the angular velocity as the object's moment of inertia will typically shrink on the order of 10^{10} to 10^{14} times during this collapse. Therefore, even if the original star was rotating relatively slowly, the compact object it leaves behind will be spinning with very high angular rates. After the compact objects' formation, however, they can decelerate (primarily through electromagnetic emission [10, 11]) so that most observed neutron stars spin with frequency on the order of 10-300 Hz. Some rapidly rotating neutron stars can reach much higher frequencies, however, with the fastest spinning neutron star known to date being PSR J1748–2446ad which rotates at a rate of 716 Hz [12].

Considering the theory parameters, however, these rates are not so large with respect to the characteristic scale of the angular rate, given by

$$\Omega_0 = \sqrt{\frac{MG}{R_S^3}}, \tag{36}$$

where M and R_S are the mass and the radius of the static configuration. Eq. (36) sets the scale for the angular rates at which acceleration due to the object's rotation becomes compatible to that from its gravity. For most neutron stars "fast rotation" corresponds to frequencies in the range 1100-2300 Hz, which places even PSR J1748–2446ad in the relatively slow spin regime as compared to this scale, since $\Omega/\Omega_0 \cong 0.3 - 0.6$ for it depending on the EOS assumptions. For

most neutron stars, this ratio is on the scale 0.1-0.3 which allows us to use it as an expansion parameter for corrections from the rotation. There are methods for non-perturbative numerical solution through consecutive iterations of corrections to the static metric with the most famous one being the so called Komatsu-Eriguchi-Hachisu (KEH) method [13].

Within the dissertation, a perturbative approximation has been used, following the standard Hartle procedure from 1967–1973 [14, 15, 16]. Since all object explored numerically fall within the slow rotation category, we follow his work only to the first order. Therefore, the metric approaches (26) as

$$dS^2 = -e^{2\Gamma}dt^2 + e^{2\Lambda}dr^2 + r^2(d\theta^2 + \sin^2\theta d\varphi^2) - 2r^2\omega\sin^2\theta dt d\varphi + O(\Omega^2), \tag{37}$$

where to first order, Γ, Λ and ω depend only on the radial coordinate r. The term $O(\Omega^2)$ is in fact shorthand for the dimensionless ratio $(\Omega/\Omega_0)^2$, which for most known neutron stars is on the order of 1–5 % correction as compared to the first order term. Given the error in measurement of most other physical characteristics of neutron stars, this is a sound approximation to make in order to keep the computations more managable!

After using the anzatz (37) in the field equations (5) with the perfect fluid energy-momentum tensor (22), one finds that the only non-trivial equations at first order are those for the component $R_{03} = R_{30}$ which yield

$$\frac{1}{r^4}\frac{d}{dr}\left(r^4 e^{-\Gamma-\Lambda}\frac{d\bar{\omega}}{dr}\right) + \frac{4}{r}\frac{d}{dr}(e^{-\Gamma-\Lambda})\bar{\omega} = 0, \tag{38}$$

where $\bar{\omega} = \Omega - \omega$ and Ω is the surface angular velocity. The solution outside of the compact object (given the vacuum solution for axis-symmetric space-time) is given by

$$\bar{\omega} = \Omega - \frac{2J}{r^3}, \tag{39}$$

where J is the total angular momentum of the compact object. Equation (39) allows us to find the moment of inertia for the compact object, which is a constant to first order in Ω. At higher orders, the angular rate deforms the neutron star and changes the moment of inertia, but given that these corrections are of order $O(\Omega^3)$ – they contribute to no more than 2 % correction to the moment of inertia for most known pulsars.

The Hartle procedure, both to first and to higher orders in Ω, can be carried in the same general way for alternative theories of Gravity, which has been performed for the TMTC case in Chapter 5 of the dissertation. The obtained equation is similar to (38), but with some additional sources generated by the different fields and further non-linear terms in the theory of choice. Unlike the classical procedure described in [14, 15, 16], however, one must consider additional radial and angular perturbations to the respective theory fields at second order, which has not been performed in the dissertation due to the precision argument outlined above and the significant technical difficulty of that task.

3.3.3 The metric outside of compact objects - ISCO, orbital and epicyclic frequencies

Due to their relatively small sizes, many compact object characteristics cannot be directly measured. One of the most abundant sources of data for them are the X-ray emissions of them and high speed orbiting matter around them. Observatories such as NICER, LOFT and SKA [17, 18, 19] can give us important data for neutron stars in close binaries with less compact objects such as white dwarfs or main sequence stars, due to the high likelihood of accretion in such systems. Such an accretion is characterized by the innermost stable circular orbit (ISCO) because it determines the boundary region where the accreting matter can no longer orbit the

compact object under gravity alone. Apart from the ISCO radius, the characteristic frequencies of oscillation for particles on stable circular orbits undergoing some small perturbations around it are an important characteristic. These are called epicyclic frequencies. There are many theories regarding the origin of some quasi-periodic oscillations (QPOs) observed in the X-ray light curves of accreting compact objects with no consensus (see [20] for a comprehensive review), but all of them include the ISCO and epicyclic frequencies as key parameters which determine these features, however.

For a general stationary axially-symmetric metric $g_{\mu\nu} = g_{\mu\nu}(r, \theta)$, the line element is given as

$$dS^2 = g_{tt}dt^2 + g_{rr}dr^2 + g_{\theta\theta}d\theta^2 + 2g_{t\varphi}dtd\varphi + g_{\varphi\varphi}d\varphi^2. \tag{40}$$

In this notation, the ISCO and epicyclic frequencies can be found by analysing the orbital motion for massive test particles. It is easy to show that there are two constants of motion generated by the timelike and axial killing vectors $E = -u_t$ and $L = u_\varphi$. Raising these we obtain for the contravariant components of a particle's 4-velocity

$$\frac{dt}{d\tau} = \frac{Eg_{\varphi\varphi} + Lg_{t\varphi}}{g_{t\varphi}^2 - g_{tt}g_{\varphi\varphi}}, \tag{41}$$

$$\frac{d\varphi}{d\tau} = -\frac{Eg_{t\varphi} + Lg_{tt}}{g_{t\varphi}^2 - g_{tt}g_{\varphi\varphi}}. \tag{42}$$

The 4-velocity's normalization condition for timelike observers $g_{\mu\nu}u^\mu u^\nu = -1$, can then be rewritten in the form

$$g_{rr}\dot{r}^2 + g_{\theta\theta}\dot{\theta}^2 + E^2U(r, \theta) = -1, \tag{43}$$

where we have defined the potential

$$U(r, \theta) = \frac{g_{\varphi\varphi} + 2lg_{t\varphi} + l^2g_{tt}}{g_{t\varphi}^2 - g_{tt}g_{\varphi\varphi}}, \tag{44}$$

using the proper orbital angular momentum $l \equiv L/E$. In the equatorial plane ($\theta = \pi/2$) this result is further reduced to an effective 1D problem $\dot{r}^2 = V(r)$ with effective potential

$$V(r) = \frac{1}{g_{rr}}\left[-1 - E^2U\left(r, \theta = \frac{\pi}{2}\right)\right]. \tag{45}$$

For some fixed E and L, the stable circular orbit at some coordinate radius r_0 is given by the conditions $V(r_0) = V'(r_0) = 0$ and $V''(r_0) > 0$, while the radius of the ISCO is given by the marginal stability condition $V''(r_0) = 0$. The orbital angular velocity of massive particles in the geometry can be found from the geodesic equations written in their Lagrange-Euler form

$$\frac{d}{d\tau}\left(g_{\mu\nu}\frac{dx^\nu}{d\tau}\right) = \frac{1}{2}\partial_\mu g_{\nu\sigma}\frac{dx^\nu}{d\tau}\frac{dx^\sigma}{d\tau}. \tag{46}$$

The radial component of these equations ($\mu = 1$) reads

$$\partial_r g_{tt}\left(\frac{dt}{d\tau}\right)^2 + 2\partial_r g_{t\varphi}\frac{dt}{d\tau}\frac{d\varphi}{d\tau} + \partial_r g_{\varphi\varphi}\left(\frac{d\varphi}{d\tau}\right)^2 = 0, \tag{47}$$

which is transformed into a quadratic algebraic equation for the orbital angular velocity $\Omega_p = d\varphi/dt = u^\varphi/u^t$. The two solutions are easily found to be

$$\Omega_p = \frac{d\varphi}{dt} = \frac{-\partial_r g_{t\varphi} \pm \sqrt{(\partial_r g_{t\varphi})^2 - \partial_r g_{tt}\partial_r g_{\varphi\varphi}}}{\partial_r g_{\varphi\varphi}} \tag{48}$$

corresponding to prograde and retrograde orbits with respect to the star's rotation. The follow-up computations (and those in the dissertation) are considered for the prograde case as the retrogade one's angular velocity is always lower and stability is lost further out from the star.

For a particle on a stable circular orbit, small radial or angular perturbations will cause periodic oscillations about the potential's minimum (with respect to r or θ). These frequencies are known as the radial and vertical epicyclic frequencies and can be found by investigating time-dependent perturbations of a stable equatorial circular orbit in the form

$$r(t) = r_0 + \delta r(t), \quad \theta(t) = \frac{\pi}{2} + \delta\theta(t). \tag{49}$$

Inserting (49) into the equation of motion (43) and assuming $\delta r \propto e^{i\omega_r t}$, $\delta\theta \propto e^{i\omega_\theta t}$ yields

$$\omega_r^2 = \frac{(g_{tt} + \Omega_p g_{t\varphi})^2}{2g_{rr}} \partial_r^2 U\left(r_0, \frac{\pi}{2}\right), \tag{50}$$

$$\omega_\theta^2 = \frac{(g_{tt} + \Omega_p g_{t\varphi})^2}{2g_{\theta\theta}} \partial_\theta^2 U\left(r_0, \frac{\pi}{2}\right), \tag{51}$$

for the radial and vertical angular epicyclic frequencies ($\omega_i = 2\pi\nu_i$). Given the interpretation of these frequencies and the proportionality between ω_r and $\partial_r^2 U(r_0, \pi/2)$, it is clear that the radial epicyclic frequency must be zero at the ISCO radius, real for $r > r_{\rm ISCO}$ and imaginary for $r < r_{\rm ISCO}$, in physical agreement with standard stability analysis conventions. Furthermore, the vertical epicyclic frequency is equal to the orbital one $\omega_\theta = \Omega_p$ for the static case ($\Omega = 0$).

Note that the definition of ISCO as well as equations (48), (50) and (51) did not make any assumptions on the underlying field equations. They are valid for a general metric theory of gravity as long as the additional fields are not coupled to the motion of matter directly (i.e. the same geodesic equations hold for the given metric). Of course, when considering theories with fields coupled to the metric (such as the TMSTs or STTs), one must compute all derivatives and quantities using the physical (Jordan) frame metric components $\tilde{g}_{\mu\nu}$. This can lead to some quantitative new effects in the structure of accretion discs around neutron stars in alternative theories since the orbital angular velocity (48) can turn imaginary (i.e. no stable circular orbit exists) in regions outside of the star, before the appearance of a true ISCO. This effect and its implications are commented from a qualitative standpoint in the dissertation.

3.4 Universal relations for compact objects

A known obstacle in the study of modified theories of gravity through neutron stars has been the ambiguity in the Equation of State (EOS) governing their internal structure. While the EOS for nuclear matter bellow the saturation density is well constrained experimentally, the central regions of neutron stars reach higher densities under which the exact state of matter is not yet well understood as already discussed in 3.2.

It is apparent from figure 1 that key characteristics such as the mass-radius relation are heavily influenced by the choice of EOS. As it has been shown in the dissertation, one can often expect similar changes to the characteristics of compact objects analysed for a single EOS but in alternative theories of gravity compared to GR, making the distinction in observations very challenging. In order to address this issue, several universal relations between properties of neutron stars were proposed and are now considered standard. What is meant by a universal relation is some quantity derived from physical properties, which to a very high accuracy does not depend on the equation of state and provides a means to probe the gravitational theory independently of the underlying nuclear matter. Two such universal relations have been explored in the dissertation, whoch have already been proven for General Relativity [21, 22], as well as some alternative theories of gravity [23, 24, 25]. It is especially interesting when

a universal relation holds independently of EOS in many theories but has different values depending on these theories. Part of the author's original results was to prove that the same relations hold in TMSTs and that they provide not only a way to distinguish between theories, but also between neutron stars with different topological charges and theory parameters within the same class of theories.

Both of the considered universal relations relate the moment of inertia, mass and radius of the stars, forming dimensionless ratios. The first of them is a fourth order polynomial fit with zero second and third order terms for the normalized moment of inertia $\tilde{I} = I/MR^2$ as a function of the compactness M/R [21, 22]

$$\tilde{I}_{\text{fit}} = \tilde{a}_0 + \tilde{a}_1 \frac{M}{R} + \tilde{a}_2 \left(\frac{M}{R}\right)^4 . \tag{52}$$

The second one relates an alternative normalization of the moment of inertia, namely $\bar{I} = I/M^3$, which is fitted with a polynomial function inverse in compactness given by the form [22]

$$\bar{I}_{\text{fit}} = \bar{a}_1 \left(\frac{M}{R}\right)^{-1} + \bar{a}_2 \left(\frac{M}{R}\right)^{-2} + \bar{a}_3 \left(\frac{M}{R}\right)^{-3} + \bar{a}_4 \left(\frac{M}{R}\right)^{-4} . \tag{53}$$

Note that both of these are in fact dimensionless, since in natural units mass and radius have the same dimensionality. In both (52) and (53), the coefficients $\tilde{a}_i$ and $\bar{a}_i$ to a very high accuracy do not depend on the EOS (typically to a few % as it has been shown for TMSTs as well).

In addition to (52) and (53), two additional universal relations which hold at the maximum mass point of a NS branch for a given EOS have been explored in the dissertation. This new class of universal relations was originally proposed and proven to hold for General Relativity in [26]. Further universal relations exist both in General Relativity and in alternative theories of gravity, relating additional parameters of rotating stars such as the well-known I-love-Q relations [27].

3.5 Gravitational waves from binary systems

One of the most interesting novel predictions of General Relativity as compared to Newtonian gravity was the presence of gravitational radiation and the inherent loss of gravitational energy to such emissions in any gravitationally bound many-body system. The energy of these waves is negligible compared to the mass of the compact objects generating them, so that they can be treated perturbatively in the post-Newtonian expansion. An excellent step-by-step treatment in GR can be found in [28].

Unlike electromagnetic waves where the leading order of the waves is dipole, the gravitational dipole moment is equivalently 0 in General Relativity (in the absence of negative energy density). To the first PN approximation, one can show that gravitational waves perturbations to the spatial components of the metric are proportional to the second time derivative of the source's quadrupole moment in the so called TT gauge (transverse trace-free gauge)

$$h^{jk}_{\text{TT}} = \frac{2G}{c^4 r} \ddot{\mathcal{I}}^{jk}_{\text{TT}}(\tau) + O\left(\frac{v_c}{c}\right)^2 , \tag{54}$$

where τ is the so called retarded time, taking into account the wave travel time along its path from the source $\tau = t - r/c$. The TT quadrupole moment itself to this order is computed by the integral

$$\mathcal{I}^{jk}_{\text{TT}} = \int_{\mathcal{M}} \rho(\tau, \vec{x}') \left(x'^j x'^k - \frac{1}{3}\delta^{jk} r^2\right) d^3x' + O\left(\frac{v_c}{c}\right)^2 , \tag{55}$$

In this context, v_c is some characteristic speed for the space-time based on which the PN approximation is performed and r is the distance to the source. Integration of (55) is performed over a 3-dimensional hypersurface $\mathcal{M}$ characterized by the constant time τ and bounded externally by some characteristic radius beyond which the density ρ in the integral is effectively zero. Treating the problem of radiation reaction in the same PN context, one can show that the total energy of the system must decrease due to the transmitted gravitational waves to first order as

$$\frac{dE}{dt} = -\frac{G}{5c^5} \dddot{\mathcal{I}}^{jk}_{\mathrm{TT}} \dddot{\mathcal{I}}^{jk}_{\mathrm{TT}} + O\left(\frac{v_c}{c}\right)^7. \tag{56}$$

The quadrupole moment tensor is not directly computed in practice from the energy density of the space-time, almost all applications treat the compact objects as point masses due to the negligible effects from their individual deformations except in the final inspiral phases. The average orbital energy lost per orbit in a two-body system, where only the orbital motion is taken into account (no individual deformations) is given by [29]

$$\left\langle \frac{dE}{dt} \right\rangle = -\frac{32}{5} \frac{G^4 m_1^2 m_2^2 (m_1 + m_2)}{c^5 a^5 (1 - e^2)^{7/2}} \left(1 + \frac{73}{24} e^2 + \frac{37}{96} e^4\right), \tag{57}$$

where m_1 and m_2 are the masses of the two orbiting objects, e is the eccentricity of their relative orbit, a is the semi-major axis, while G and c are respectively the gravitational constant and the speed of light.

Of course, this energy loss is not directly measurable, but its effect on the system is to decrease the gravitational energy and for the objects to spiral closer towards each-other. Many alternative theories of gravity predict some additional channels of energy loss such as non-zero dipole moment due to additional fields, which leads to a much larger orbital energy loss. It is precisely the observation of the orbital period evolution for binary systems which has led to some of the first and most strict constraints on alternative theories of gravity [30, 31, 32].

In Chapter 8 of the dissertation, this measured change of the orbital period for the binary systems $\dot{P}_b$ has been used as compared to the simulation's predictions has been used as a basis for the likelihood function used in the Bayesian analysis. Considering the dependence of the orbital period P_b on the semi-major axis a as well as the latter's evolution based on (57) and its derived equations from [29], one can show that the orbital decay due to the quadrupole energy loss amounts to

$$\dot{P}_b^{\mathrm{quad}} = -\frac{192\pi G^{5/3}}{5c^5} f(e) \left(\frac{2\pi}{P_b}\right)^{5/3} \frac{m_p m_c}{(m_p + m_c)^{1/3}}, \tag{58}$$

where the notation has been switched to pulsar and companion masses m_p and m_c respectively in anticipation of the observations to be used, and an auxiliary function of the eccentricity has been defined as

$$f(e) \equiv \left(1 + \frac{73}{24} e^2 + \frac{37}{96} e^4\right) (1 - e^2)^{-7/2} \tag{59}$$

for simplicity of the notation.

One can derive the equivalent contributions for alternative theories of gravity as well as their dipole terms (if existing). Following [2], one can show that STTs for example give rise to a dipole moment contribution for the orbital decay given by

$$\dot{P}_b^{\mathrm{dipole}} = -\frac{2\pi G_*}{c^3} g(e) \left(\frac{2\pi}{P_b}\right) \frac{m_p m_c}{m_p + m_c} (\alpha_A - \alpha_B)^2, \tag{60}$$

where all quantities have the same meaning as in (58) with the addition of the neutron star scalar and companion scalar couplings α_A and α_B and a second auxiliary function of the eccentricity

$$g(e) \equiv \left(1 + \frac{e^2}{2}\right)(1 - e^2)^{-5/2}. \tag{61}$$

The scalar coupling for an object with mass m_A is defined as the derivative

$$\alpha_A \equiv \frac{\partial \ln m_A}{\partial \varphi_\infty}, \tag{62}$$

where the baryonic mass of the object is fixed when taking the derivative and φ_∞ means the asymptotic value of the field.

(60) has been modified accordingly in the dissertation to the equivalent coupling for scalar-Gauss-Bonnet theory while (58) has been used directly, taking into account only the different meaning of the gravitational constant in the Gauss-Bonnet theory, in order to form the likelihood function with respect to $\dot{P}_b$ observations. These functions are the basis of the likelihood function formed in order to constrain the parameters of the theory through Bayesian probabilistic analysis.

4 Numerical Methods

Obtaining the original results of the dissertation has only been possible through multiple numerical methods, required due to the non-linearity of the problems to be solved. Most of these methods have been implemented by the author in C or Python programming languages and optimized for the specifics of the problems. An exception is the Markov Chain Monte Carlo (MCMC), where an existing library has been used [33]. In the remaining cases [34] has been used as a primary reference for the mathematical formulation and implementation details with some touch of the author based on the problem specifics.

Interpolations

When working numerically with the various equations, the actual manipulations are performed on arrays with finite number of samples. The primary method of interpolation used is cubic spline, which constructs a cubic polynomial approximating the function in each region between the tabulated points. This method is preferred since the obtained interpolating function is C^2 smooth and it is relatively easy to obtain while maintaining high accuracy.

Numerical differentiation and integration

Standard methods of approximation for the derivative of a function through finite differences have been used when carrying out numerical differentiation and integration. A derivative of accuracy $O(h^4)$ with respect to the numerical step h has been used to carry out the differentiation, using an interpolation of the function in order to obtain an optimal step with respect to the machine precision and rounding error. The trapezoid and Simpson's methods have been used to carry out integration. The latter's error drops by the 4th power of the number of points as $O(1/N^4)$ which is negligible for the purpose of the definite integrals computed in the dissertation problems.

Algebraic equations

Finding roots to algebraic equations of the kind $f(x) = 0$ has been accomplished through the combination of two methods: Newton-Raphson and bisection methods. The first of these is

much faster to converge, but is not globally stable and can lead to unstable loops while the second one always converges to at least one root in an interval where such exists, although it is considerably slower. The core of Newton's method is to linearise the function near a root and use consecutive linear approximations in order to reach the root with the desired precision. On the other hand, the bisection method is a consecutive division of the original interval where a root is contained (i.e. the function has different signs on the two ends of that interval) until this interval reaches a width compatible with the desired accuracy. In practice, Newton's method has been used as a primary such in the dissertation, but when it appears to be diverging, several bisection iterations are taken in order to avoid it. In the cases of multi-dimensional root search, the bisection is not directly applicable, which has led to the use of a regularized cost function when using non-linear least squares in the dissertation.

Numerical integration of ODE systems

Numerically solving Ordinary Differential Equations (ODEs) is central to finding the structure of self-gravitating bodies. This type of differential equations are stiff – they may require a very small step to avoid numerical jump to a nearby solution which is changing much faster than the one desired. In order to keep the desired accuracy without slowing the code too much, and to accommodate integration of the structure equations all the way to the space-time asymptotics, the author has used an adaptive-step Dormand-Prince method [35]. This method is a special case of a Runge-Kutta method with embedded error estimation which allows for the evaluation of the necessary step in order to ensure a certain accuracy. The step is controlled by a proportional-integral (PI) controller which uses the weights between two consecutive steps in order to avoid making changes too rapidly while maintaining the required accuracy. This method is preferred by the author as compared to other similar methods (such as the widely used Fehlberg and Cash–Karp methods), since two of the coefficient rows for the Dormand-Prince Butcher Tableu are the same, reducing the number of required computations per step for the same final accuracy.

Shooting method

In many practical problems one does not know an initial value but a boundary value. As an example, when computing the structure equations, one does not know the central values of the function Γ and the different fields but their asymptotics are well known. In these cases, the author has used the shooting method, which solves an algebraic equation for finding the right initial value of a given parameter, treating the numerical integration itself as a non-linear function mapping this initial value to the boundary value. The name of this method comes precisely from the analogy with shooting, where the initial angle of shooting is changed based on how much the target is "missed".

Non-linear least squares

Many physical models require fitting of different functions to some expected analytical behaviour. In most cases, there are some measured points $\{x_i\}$ and $\{y_i\}$, which are expected to obey some law, but which contain noise due to the measurements or some external influences interfering with that law, so that they do not follow it precisely. In such cases, the author has used a fitting method, which in the case of the universal relations could be both linear and non-linear. The fitting function is typically given in a parametric form $y = f(x|\vec{a})$, where the parameters $\vec{a}$ are found in such a way as to describe the experimental data best. This means that the problem is equivalent to finding the local minimum of some function which gives the mean deviation measure between each of the experimental points $\{y_i\}$ and the predictions of

the function $f(x_i)$. The least squares method (as its name suggests), this deviation measure is given by the sum of the squares between the error terms for each point. Finding the best fit is equivalent to minimizing this function, which can be accomplished by finding a root of its derivative. Of course, strongly non-linear functions may have multiple local minimums and so the success of this task strongly depends on both the choice of a fitting function and the initial conditions choice for the Newton-Raphson method which has been used to find the root of the resulting non-linear derivative function. Throughout the dissertation, the Levenberg-Marquardt method [36] has been used, in order to regularize the problem with a Lagrange multiplier dependent on the step, instead of optimizing the standard cost function, leading to better convergence close to inflex points.

Markov Chain Monte Carlo (MCMC)

The Markov Chain Monte Carlo (MCMC) is a method for random sampling. Like other Monte Carlo methods, it can be used to evaluate higher dimensional integrals in a given region of the space of variables. Unlike more traditional Monte Carlo methods, however, the function is sampled based on its values in the given region, while classical methods sample homogeneously. This is especially useful when working with Bayesian analysis – this method allows us to optimize significantly the number of sampled points in order to reach a given accuracy, since the probability for a given point to be sampled is proportional to its value. In other words, given a likelihood function which should be normed, the integration will be carried out in an optimal way, including the most important parts (where the probability is highest) first and with higher frequency, which can be very important in terms of computing speed when dealing with more than 3 parameters of the distribution. The dissertation makes use of the library `emcee` from [33]. It utilizes an affine-invariant ensemble sampler described in [37], which further improves the MCMC by utilizing appropriate rescaling of the parameters (affine transformation) to deal with distributions skewed in some of their parameters.

5 Slowly rotating topological neutron stars and their universal relations

Universal relations and some of the most important observational properties of slowly rotating compact objects in a certain class of Tensor-Multi-Scalar Theories (TMST) of Gravity have been explored in the dissertation. A new type of compact objects called topological neutron star was shown to exist in TMST [4] ([38] for scalarization in such theories). Two types of universal relations connecting the appropriately normalized moment of inertia and the compactness of the objects have been evaluated for these compact objects. These relations were examined in the GR case in [21, 22]. They were later generalized to the case of $f(R)$ and scalar-tensor theories with a massive scalar field [23, 24, 25]. The methodology outlined in these works has been followed and the author has compared the topological neutron star results with the GR case for several Equations of State (EOS) and at several theory parameters for two coupling functions. A piecewise polytropic approximation of several realistic nuclear matter equations of state [8] has been used to obtain these results. These are the APR4 and SLy, that fit very well to the current observational constraints, as well as several higher/lower stiffness and maximum mass equations of state (MS1, MPA1, APR2, H4) in order to check the universality of the relations. The complete results are published in [39].

5.1 Structure equations and methodology

The theory of section 2.2 has been followed, using a gravitational interaction mediated by the spacetime metric $g_{\mu\nu}$ and N scalar fields φ^a with values in a coordinate patch of an N-dimensional Riemannian (target) manifold $\mathbb{E}^N$ with a positive-definite metric $\gamma_{ab}(\varphi)$ defined on it. The Einstein frame action of the theory and the resulting field equations for the static case are given by (6) and (7) respectively. The static spherical solution has been perturbed by a term scaling as $O(\Omega)$ in the Einstein frame, following the general methodology outlined in 3.3.2 for a Hartle procedure with line element (37).

Following the previous work on topological neutron stars [38], the target space for the TMST has been chosen as the round three-dimensional sphere $\mathbb{S}^3$ with line element

$$\gamma_{ab}d\varphi^a d\varphi^b = a^2\left[d\chi^2 + \sin^2\chi(d\Theta^2 + \sin^2\Theta d\Phi^2)\right], \tag{63}$$

defined by a radius $a > 0$ and the standard angular coordinates χ, Θ, Φ on the sphere. The motivation behind this choice is the fact that $\mathbb{S}^3$ is among the simplest target spaces that permit the existence of spherically symmetric topological neutron stars. Some further assumptions have been done to simplify the target space solutions. Considering that the χ field depends only on the radial coordinate ($\chi = \chi(r)$) and that the Θ and Φ fields depend only on the corresponding angular coordinates ($\Theta = \Theta(\theta)$ and $\Phi = \Phi(\phi)$) leads to unique solutions of the latter two, compatible with the spherical symmetry of the structure equations. These solutions are $\Theta = \theta$ and $\Phi = \phi$ as shown in [4].

Static structure equations

Under these simplifying assumptions, one can easily derive the structure equations for the static configuration. Using the theory field equations (7) and the EM tensor conservation law (9), the structure equations take the form

$$\frac{2}{r}e^{-2\Lambda}\Lambda' + \frac{1}{r^2}\left(1 - e^{-2\Lambda}\right) = 8\pi G_* A^4(\chi)\tilde{\varepsilon} + a^2\left(e^{-2\Lambda}\chi'^2 + 2\frac{\sin^2\chi}{r^2}\right) + 2V(\chi), \tag{64}$$

$$\frac{2}{r}e^{-2\Lambda}\Gamma' - \frac{1}{r^2}\left(1 - e^{-2\Lambda}\right) = 8\pi G_* A^4(\chi)\tilde{p} + a^2\left(e^{-2\Lambda}\chi'^2 - 2\frac{\sin^2\chi}{r^2}\right) - 2V(\chi), \tag{65}$$

$$\chi'' + \left(\Gamma' - \Lambda' + \frac{2}{r}\right)\chi' = \left[2\frac{\sin\chi\cos\chi}{r^2} + \frac{1}{a^2}\frac{\partial V(\chi)}{\partial\chi} + \frac{4\pi G_*}{a^2}A^4(\chi)\frac{\partial \ln A(\chi)}{\partial\chi}(\tilde{\varepsilon} - 3\tilde{p})\right]e^{2\Lambda}, \tag{66}$$

$$\tilde{p}' = -(\tilde{\varepsilon} + \tilde{p})\left[\Gamma' + \frac{\partial \ln A(\chi)}{\partial\chi}\chi'\right], \tag{67}$$

Apart from the standard boundary conditions for the metric functions derived from asymptotic flatness $\Gamma(\infty) = \Lambda(\infty) = 0$ and regularity at the center $\Lambda(0) = 0$, similar regularity is also required from the scalar field equations. This leads to the conditions $\chi(\infty) = k\pi$ and $\chi(0) = n\pi$ with both k and n being integers: $k, n \in \mathbb{Z}$. The former condition can be set to zero without loss of generality to $k = 0$. Since $\chi(\infty) = 0$, the extension of the map $\phi : \Sigma \to \mathbb{S}^3$ is topologically equivalent to the map $\phi : \mathbb{S}^3 \to \mathbb{S}^3$, and it can be shown that n is its degree [4]. Thus the solutions with $n \neq 0$ are topologically nontrivial.

The investigation has been focused on two different coupling functions characterized by a single dimensionless parameter β. The first one is that originally used in [4] given by

$$A(\chi) = e^{\beta\sin^2\chi}, \tag{68}$$

while the second one is a monotonic function of χ

$$A(\chi) = e^{\frac{1}{2}\beta\chi^2}. \tag{69}$$

The two functions approach each-other as $\chi \to 0$ but as it is shown in the dissertation – they lead to very different behaviour. Solutions of the static topological neutron stars are obtained by setting the appropriate central conditions for Λ, $\tilde{\varepsilon}$ and χ and then performing a shooting method to determine $(d\chi/dr)|_0$ and $\Gamma(0)$ from the asymptotics of χ and Γ which are used as boundary conditions. For the numerical integration of the differential equations an adaptive Dormand-Prince embedded error estimation method has been implemented by the author in accordance with 4.

The mass-radius relations for topological neutron stars is shown in Fig. 2a for the non-monotonic coupling function (68). In this case stable solutions exist both for $n = 1$ and $n = 2$ topological charges (excluding the case $\beta = 0.04$ where the $n = 2$ solutions appear after the branch's maximum mass). Fig. 2b on the other hand presents the mass-radius relations for the monotonic coupling function (69) where stable solutions exist only for $n = 1$ topological charge and in a much smaller range of β (around $\beta = -0.01$).

It was shown in [4] that other branches of solutions exist as well for a fixed coupling function and values of n and β, but all of them are unstable against radial perturbations [38] and we will not comment on them further.

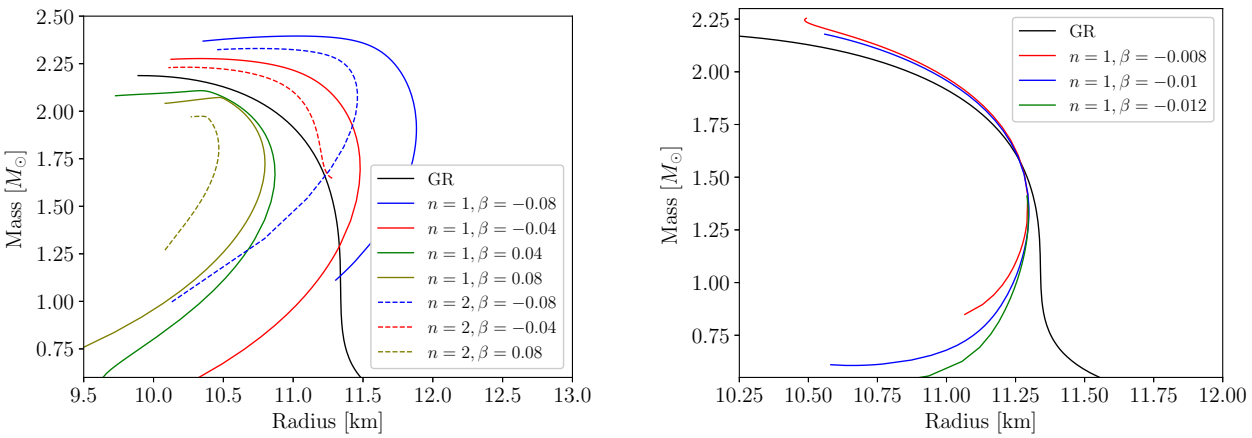

(a) Coupling function (68)

(b) Coupling function (69)

Figure 2: Mass-radius relations for the APR4 EOS and different values of β for the coupling functions (68) (on the left) and (69) (on the right). $n = 1$ solutions are shown with solid lines while $n = 2$ solutions are indicated with dashed lines of the same color (the latter exist only for the nonmonotonic coupling function)

It is easy to notice that in general the $n = 1$ branches are more massive than their $n = 2$ counterparts (when the latter exist). Considering Fig.2a, the overall effect of negative β values is to increase the masses of the solutions with the same radius (making them more compact) while the effect of positive β values is the opposite. The actual shape of the mass-radius relation, however, is also heavily influenced by the value of the parameter and these effects are not easily predictable or monotonic in nature.

In most cases the "end" of a branch (i.e. the highest pressure for which solutions were found) has been chosen arbitrarily after the corresponding sequence's maximum mass is reached. However, in some cases the branch of solutions not only appears at some minimal central pressure but also disappears at another maximum central pressure. Such is the case for the solutions obtained for the monotonic coupling function (69) which are found in a much more

restricted range for β and central pressures. No stable or physically meaningful solutions were found for the $n = 2$ topological charge in this case and each of the three stable branches shown on Fig. 2b disappears before it reaches the maximum of the mass.

Structure equations for slow rotation

Considering the general methodology outlined in 3.3.2, the only non-trivial equation to first order in Ω is that for the Ricci tensor components $R_{03} = R_{30}$. After taking into account the static equations (64)-(67) as equalities, to first order in Ω we have

$$\frac{1}{r^4}\frac{d}{dr}\left(r^4 e^{-\Gamma-\Lambda}\bar{\omega}'\right) + \frac{4}{r}\frac{d}{dr}(e^{-\Gamma-\Lambda})\bar{\omega} + 4a^2 e^{-\Gamma-\Lambda}\bar{\omega}\chi'^2 + \frac{4a^2\omega}{r^2}\sin^2\chi e^{\Lambda-\Gamma} = 0, \tag{70}$$

where the function $\bar{\omega} = \Omega - \omega$ has been defined. The central values of the functions are $\bar{\omega}'(0) = 0$ and $\bar{\omega}(0) = \bar{\omega}_c$ with the latter determined through a shooting method in order to obtain the desired angular velocity of the star Ω. Note that Ω is actually the same in both Einstein and Jordan frames.

Having integrated (70) as per the methodology in 3.3.2, one can use its asymptotic form (39) to extract the star's angular momentum $J = I\Omega$ and thus obtain the moment of inertia along the axis of rotation. Alternatively, one can integrate the two sides of (70) leading to a conserved quantity proportional to the angular momentum. After a division by Ω, the asymptotic and integral definitions are given by

$$I_{\text{asympt}} = \lim_{r\to\infty} -\frac{1}{6} r^4 e^{-\Gamma-\Lambda}\left(\frac{d\tilde{\omega}}{dr}\right), \tag{71}$$

$$I_{\text{integral}} = \frac{8\pi G_*}{3}\int_0^{r_S} A^4(\chi)(\tilde{p}+\tilde{\varepsilon})e^{\Lambda-\Gamma} r^4(1-\tilde{\omega})dr - \frac{2a^2}{3}\int_0^{\infty} r^2\tilde{\omega}e^{\Lambda-\Gamma}\sin^2\chi dr \tag{72}$$

where $\tilde{\omega} = \omega/\Omega = 1 - \bar{\omega}/\Omega$ is the reduced angular velocity. Both definitions are implemented as part of the numerical integration to further verify the fidelity of the results and the obtained values differ from each-other with relative error consistently on the order of 10^{-11} for the various branches.

ISCO, orbital and epicyclic frequencies

The same general methodology as that outlined in 3.3.3 is followed for TMST with one major difference – all derivatives and quantities in the latter case must be computed using the physical (Jordan) frame metric components $\tilde{g}_{\mu\nu}$. This leads to a noteworthy behavior in the orbital angular velocity Ω_p as given by (48) which can turn imaginary (i.e. no stable circular orbits exist) in regions outside the star, before the appearance of a true ISCO. This can be traced to the negative term under the square root of eq. (48). In GR the derivative $\partial_r g_{tt}$ is always negative outside of the star (the metric function g_{tt} is monotonically decreasing). However, the sign of the corresponding quantity in the generalized theory $\partial_r(A^2(\chi)g_{tt}) = \partial_r\tilde{g}_{tt}$ is now determined not only by g_{tt} but also by the coupling function $A(\chi)$. It turns out that in the case of the non-monotonic coupling function (68) this leads to regions outside the ISCO where stable circular orbits do not exist and where the accretion disc may be split. This effect presents considerable interest in terms of potential observational traits but requires a more detailed study but it requires more profound exploration for complete results and has thus been left for a follow-up work. This is the reason why the outlined results for the ISCO and the epicyclic frequencies are only for the case of a monotonic coupling function at different theory parameters and angular frequencies for the topological charge $n = 1$.

5.2 Results

Moment of Inertia and universal relations

This section presents the results obtained for the moment of inertia as well as our study of two relations known to be universal (independent of EOS). These are relations between the dimensionless compactness M/R and two normalizations of the moment of inertia $\tilde{I} = I/MR^2$ and $\bar{I} = I/M^3$ described in 3.4. The results presented are only for the astrophysically relevant stable branch of topological neutron stars without commenting on the other unstable branches for which a comparison is made between GR and the branches with $n = 1$ and $n = 2$ topological charges (where present) using APR4, Sly, MS1, MPA1, APR2 and H4 equations of state for several different theory parameters.

Before considering these results for the different EOS, the following Figs. 3a and 3b show the moment of inertia as a function of the neutron star masses. The shown branches of solutions are the same as those depicted in Fig. 2a and Fig. 2b.

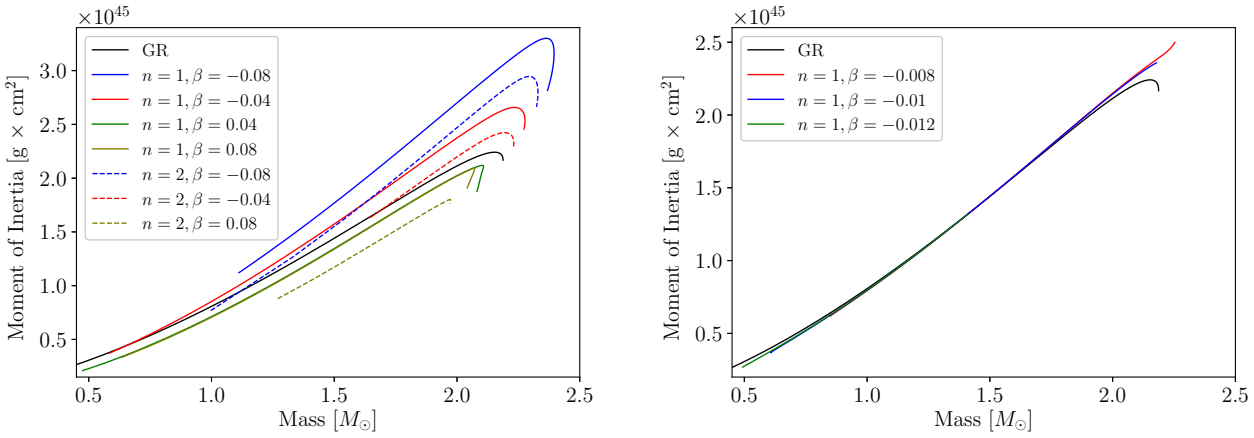

(a) Coupling function (68)

(b) Coupling function (69)

Figure 3: Moment of inertia-mass relations for the APR4 EOS and different values of β for the coupling functions (68) (left) and (69) (right). $n = 1$ solutions are shown with solid lines while $n = 2$ solutions are indicated with dashed lines of the same color. These are the same branches of solutions depicted in Fig. 2.

The behavior of the moment of inertia evidently follows what was already outlined for the mass–radius relation. The higher topological charge leads to lower masses and thus lower moment of inertia. Negative β increases the overall compactness and positive β acts in the opposite way (for the non-monotonic coupling function (68). A complete lack of maximum of $I(M)$ is observed in the case of the monotonic coupling function.

While the mass-radius and mass-moment of inertia relations are very different for the different EOS, as seen on the plots above, all of the normalized moments of inertia used in the universal relations have a very similar shape, as it will be seen further down.

We follow the fourth order polynomial fit with zero second and third order terms described by (52) for $\tilde{I} = I/MR^2$. To avoid too many cluttered plots, Fig. 4 compares the fits $\tilde{I}_{\text{fit}}$ for $\beta = -0.01$ of the monotonic coupling function (69), GR and the non-monotonic coupling function (68) at values $\beta = -0.08$ and $\beta = 0.08$. These fits are obtained using an equal number of points for each of the 6 EOS (APR4, SLy, MS1, MPA1, APR2 and H4) and fitting the functional form (52) through least squares. The numerical values of the fit parameters are presented in the dissertation and in [39].

It is evident that there is very little difference between the polynomial fits for GR and the TMST for the monotonic coupling function $A_{\text{mon}}(\chi)$ given by (69). This is not the case,

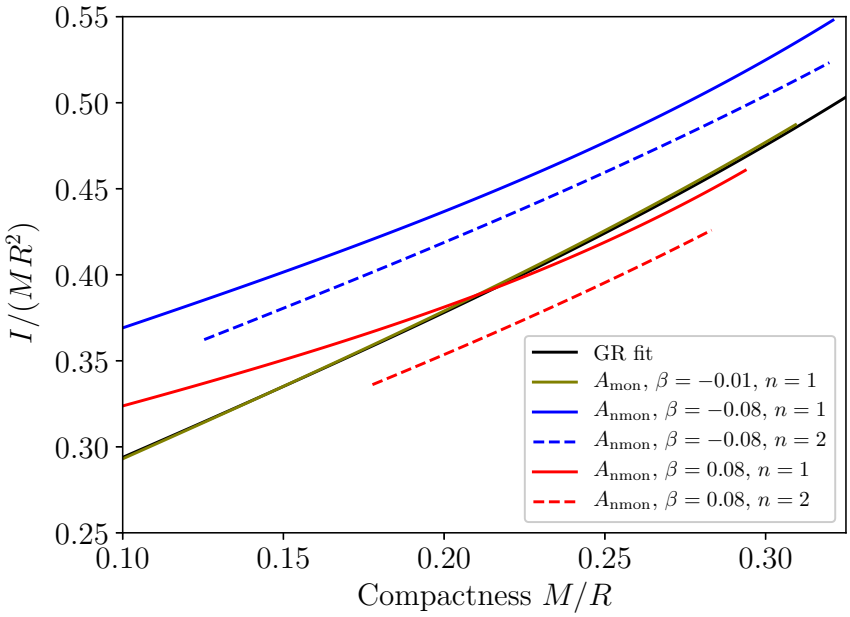

Figure 4: Comparison between the $\tilde{I}$ fits obtained through (52) for different theory parameters considered. The olive curve is that obtained for the monotonic coupling function (69) while the remaining four curves show the qualitative difference in results for positive and negative beta in the case of non-monotonic coupling (68).

however, for the non-monotonic function $A_{\rm nmon}(\chi)$ given by eq. (68) where significant differences are observed. For example in the $\beta = -0.08$ case the polynomial fit values are consistently around 20 % higher as compared to GR. The $n = 1$ fit for the positive $\beta = 0.08$ has a slightly different shape from GR particularly at lower compactness but would be hard to discern within experiments available today. The $n = 2$ solutions of the same value $\beta = 0.08$, however, lead to values of $\tilde{I}$ consistently lower by about 7%.

The second alternative normalization of the moment of inertia $\bar{I} = I/M^3$ is fitted with a polynomial function of the form (53). The numerical values of the fitting coefficients, as well as the fitting error can once again be found in the dissertation and in [39].

Fig. 5 compares the $\bar{I}_{\rm fit}$ obtained using the above formula for the same values of the parameters and equations of state as in Fig. 4. Once again, the curve for the coupling function (69) is virtually indistinguishable from the GR one and the most significant deviation is observed for the non-monotonic coupling (68) with $n = 1$ topological charge at $\beta = -0.08$ (about 20 % higher) and with $n = 2$ topological charge at $\beta = 0.08$ (about 7 % lower).

The following two Figs. 6a and 6b show the actual data points for each of the six EOS considered as well as the fits obtained from them. Only the value of $\beta = -0.08$ of the non-monotonic coupling function (68) has been shown for the purpose of better visualization. This value of β has been chosen since it presents the highest difference as compared to GR. The $n = 1$ and $n = 2$ solutions for the non-monotonic coupling function (68) are depicted with pluses ("+") and crosses ("x") and follow the colors of the GR solutions for the different EOS. The highest relative error of the fits is displayed in the bottom of the figure and it is no greater than 6% (highest for the H4 EOS). Based on the relative error of the fits, we can conclude that the EOS universality of $\tilde{I}$ as a function of the stellar compactness is fulfilled in TMST at least as well as in GR.

Similarly, as seen on the following Fig. 6b, the error between the actual results and the fit for the second normalization $\bar{I}$ does not exceed 6% with the highest maximum of the error once again visible for H4 EOS which confirms the universality of $\bar{I}$ as well for $\beta = -0.08$. The

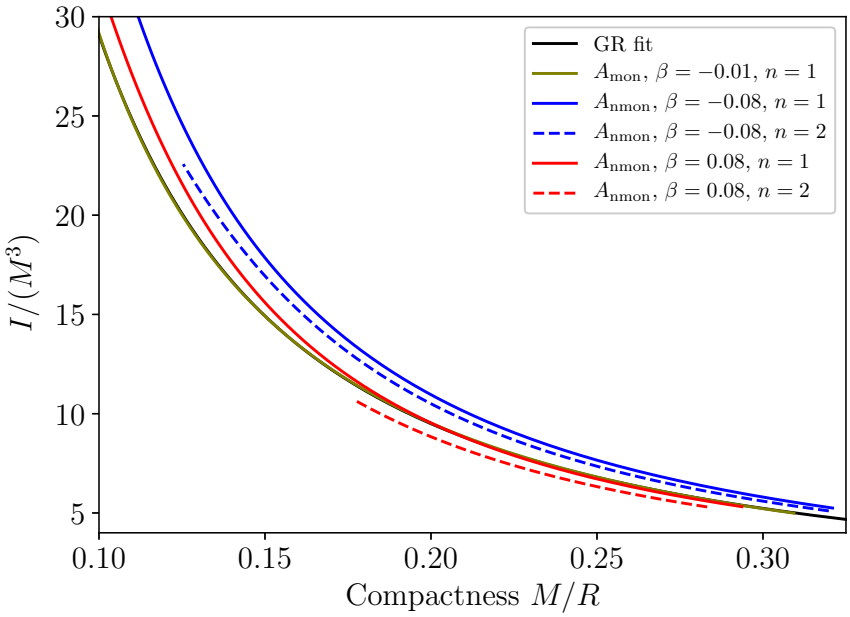

Figure 5: Comparison between the $\bar{I}$ fits obtained through (53) for different theory parameters considered. The olive curve is that obtained for the monotonic coupling function (69) while the remaining four curves show the qualitative difference in results for positive and negative beta in the case of non-monotonic coupling (68).

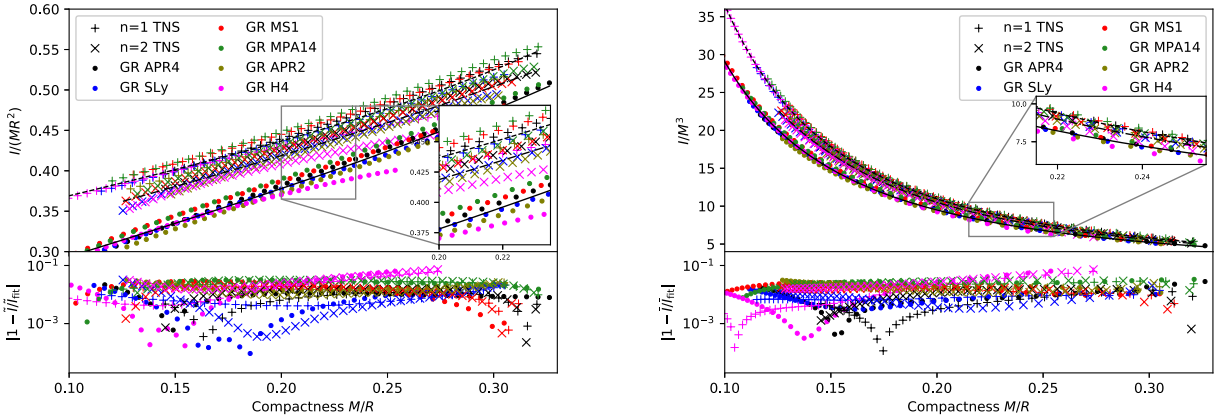

(a) Coupling function (68)

(b) Coupling function (69)

Figure 6: The normalized moment of inertia $\tilde{I}$ (left) and $\bar{I}$ (right) as a function of the compactness for GR and topological neutron stars with a coupling function (69), where we have chosen $\beta = -0.08$ as a representative plot. Dots show results for GR while pluses and crosses show results for the topological neutron stars of $n = 1$ and $n = 2$ respectively, with the same color scheme for the EOS as in GR. Solid, dashed and dash-dotted lines show the corresponding fits following eq. (52) (left) and (53) (right) for GR, $n = 1$ $n = 2$ respectively.

fits for the remaining β values and the monotonic coupling function have a relative error of the same order, confirming that the topological neutron stars of both charges $n = 1$ and $n = 2$ indeed satisfy the standard universal relations explored.

The dissertation and [39] present the numerical values for the RMS error of the fits $\tilde{I}_{\chi^2}$ and $\bar{I}_{\chi^2}$ from representative cases which show that the universality is indeed well followed.

Characteristics of electromagnetic observations

The results for the ISCO as well as the orbital and epicyclic frequencies have been obtained for static as well as $f = 80$ Hz and $f = 160$ Hz rotating neutron stars. Both of these values for the frequency place the stars at the slowly rotating regime. Unlike the moment of inertia, which is not influenced to the first order in Ω, the innermost stable circular orbit (ISCO) as well as the orbital ν_p and epicyclic frequencies ν_r, ν_θ are modified based on the star's rotation. All these results presented in the dissertation and in this summary are the corresponding physical Jordan frame quantities.

As discussed previously, the ISCO computation in the case of a non-monotonic coupling function such as (68) is not trivial and can lead to a splitting of the accretion disc outside of the star. Therefore, we have considered only the monotonic coupling function (69) while the more complicated case of non-monotonic $A(\chi)$ requires much more profound investigations and will be discussed in a future work.

Fig. 7 displays the static ISCO radius (in the physical Jordan frame) for the stable branch of topological neutron stars with $n = 1$ at different β parameters for the APR4 EOS and compares them to GR. Whenever the ISCO radius is less than the stars' radius, the latter is used (thus the visible discontinuity of the derivatives around 1.25 $M_\odot$). It is obvious that all results follow closely GR and deviations of the ISCO for any physical radii between the considered set of parameters and GR are marginal.

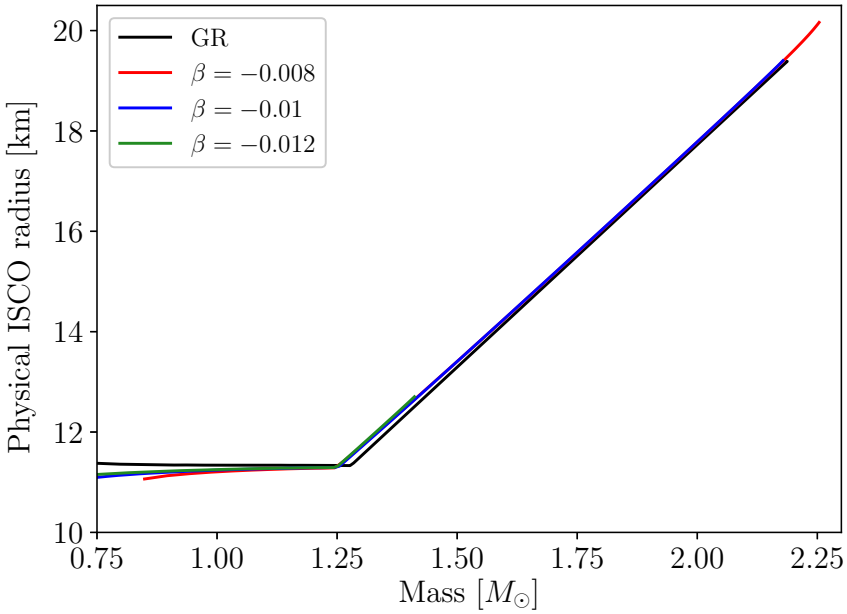

Figure 7: ISCO radius (physical) as a function of the gravitational mass for GR and TMST with the monotonic coupling function (69), for $n = 1$, different β values and $f = 0$ Hz.

More important than the actual radius of the ISCO from observational standpoint is the orbital frequency obtained at its radius. Fig. 8 presents the results for the three cases of β studied following the computation of eq. (48) in the Jordan frame of the theory at $f = 0$ Hz. Once again, deviations from GR are minor and could not be used to experimentally discern topological neutron stars.

Finally, the radial epicyclic frequency's maximum value outside of the star at $f = 0$ Hz is given in the following Fig. 9. The highest deviation is once again around 1 $M_\odot$ reaching as much as 6% and once again becoming negligible at higher masses. Since neutron stars with masses lower than that are not observed and currently considered as non-existing, the radial epicyclic

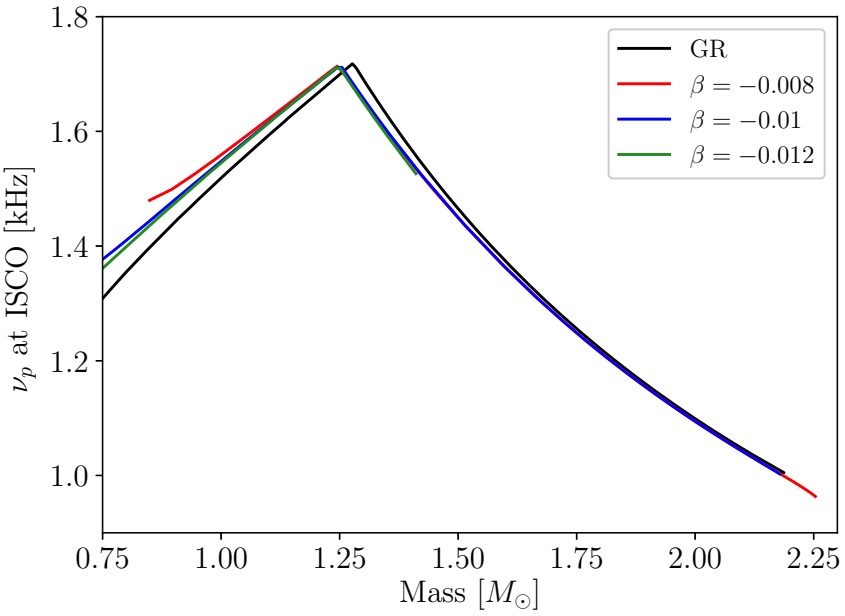

Figure 8: Orbital frequency at the ISCO radius as a function of the gravitational mass for GR and TMST with the monotonic coupling function (69), for $n = 1$, different β values and $f = 0$ Hz.

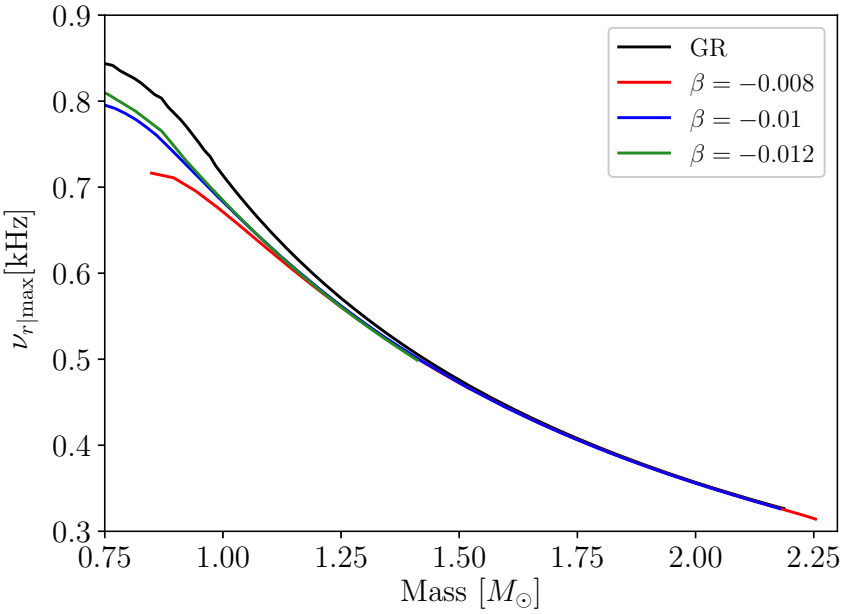

Figure 9: Maximum absolute value of the radial epicyclic frequency ν_r as a function of the gravitational mass for GR and TMST with the monotonic coupling function (69), for $n = 1$, different β values and $f = 0$ Hz.

frequency does not offer any significant observational difference between GR and topological neutron stars similarly to the orbital one.

Fig. 10 displays the same quantities in the case of slow rotation, where the solid lines corresponding to the $f = 0$ Hz case, while the dashed and dash-dotted lines give the same dependencies at $f = 80$ Hz and $f = 160$ Hz. The results are obtained in the slow rotation regime but the majority of observed neutron stars fall within this approximation. There is also

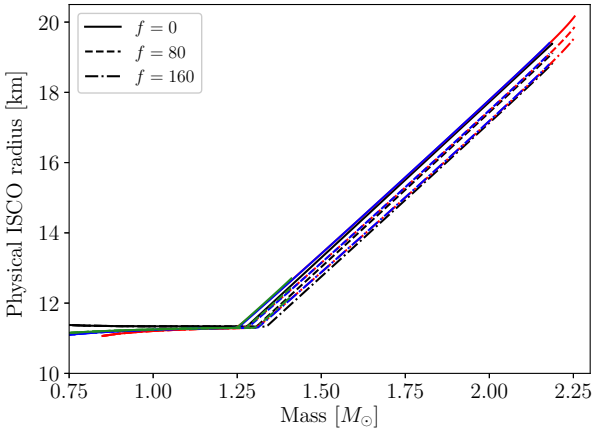

(a) ISCO radius

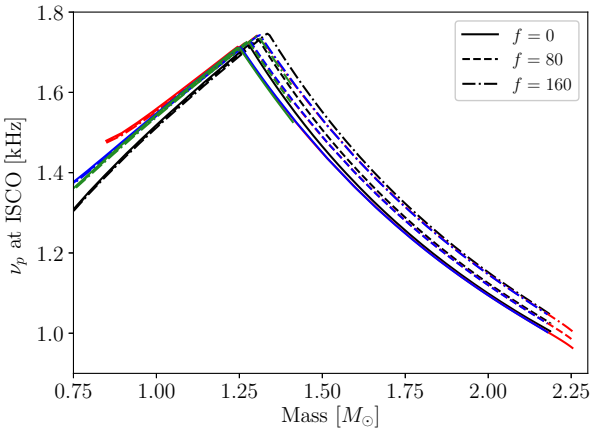

(b) Orbital frequency at the ISCO

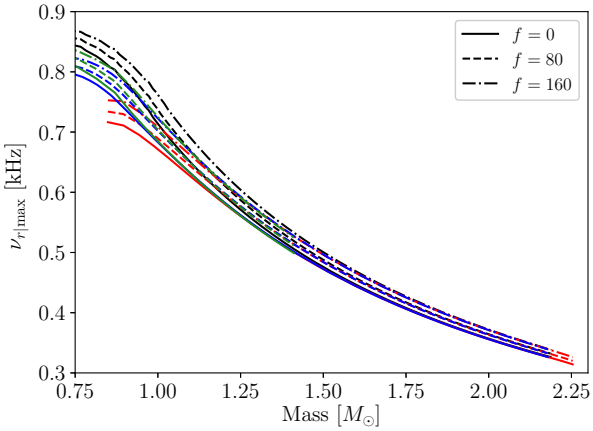

(c) Maximal radial epicyclic frequency

Figure 10: ISCO radius, orbital frequency at the ISCO and absolute value of the maximal radial epicyclic frequency ν_r as functions of the gravitational mass for GR and TMST with the monotonic coupling function (69), for $n = 1$ and different β values. Solid lines denote static configuration while dashed and dash-dotted lines correspond to the $f = 80$ Hz and $f = 160$ Hz cases. Color scheme follows Fig.7.

reason to believe that results at higher order of Ω are not qualitatively different [24].

The decrease in ISCO radius due to the star's rotation leads to an overlap between the plots in an even larger region making the GR and the topological cases harder to discern without knowing the rotational frequency precisely. For each of the rotational cases by itself, no significant distinction is possible once again. As far as the orbital and maximum radial epicyclic frequencies are concerned – no major difference can be seen between GR and the $n = 1$ topological neutron star branch with coupling function (69) for masses higher than $\cong 1.2-1.3 M_\odot$. It appears that the monotonic coupling function (69) does not predict significant qualitative or quantitative deviations from GR as far as the X-ray observations are concerned.

5.3 Commentary

The properties of topological neutron stars (TNS) have been explored in the disertation. These are a new and very interesting class of compact objects in the Tensor Multi-Scalar Theories (TMST) of gravity. These have been explored in the case of slow rotation and in addition the study of these objects' dependence on theory parameters, topological charge and coupling

functions has been extended. The main focus of the work was on the investigation of universal relations related to their moment of inertia and the quantities related to accretion under slow rotation which were not previously compared to the same quantities in GR.

The author has confirmed the EOS independence between the suitably normalized moment of inertia for the TNS and their compactness, comparing the obtained results with those for neutron stars in General Relativity. It turns out that for one of the coupling functions, showing a monotonic behavior with respect to the scalar field, these universal relations are almost indistinguishable from GR, making them not only EOS independent, but also theory of gravity independent up to a large extend. For more complicated non-monotonic functions, though, the deviations can be significant, allowing not only to distinguish between GR and TMST, but also between solutions with different values of the topological charge. This demonstrates that the future observations can help us test the very interesting hypothesis that neutron stars can posses a new property that is the topological charge.

The author has also obtained accretion-relevant properties such as the ISCO radius, orbital and epicyclic frequencies for TNS at different rotation rates, comparing them once again to the GR results. The obtained TNS quantities differ significantly from those in GR only for some coupling functions and theory parameter values which leaves several observational traits to be sought after and explored. In the case of monotonic coupling function there are no qualitative difference between GR and TMST and in addition, the qualitative deviations from GR are very small, making them practically unmeasurable. Some interesting qualitative differences appear in particular for non-monotonic coupling function for the ISCO-related quantities, where the quantitative deviations can be large as well, that will be further explored in a dedicated work as they require more profound investigations. This provides a firm reason to pursue more accurate observations and systematic studies in order to constraint alternative theory parameters in the strong regime of gravity.

6 Maximum mass point universal relations in Scalar-Tensor theories

A new type of universal relation in Scalar-Tensor Theories (STT) has been explored in the dissertation This relation was first shown to hold in the case of GR neutron stars in [26] based on an observation of L. Lindblom [40] that the high-density nuclear matter EOS can be well parametrized by two parameters only. This type of universal relations are slightly different from those described in the previous sections since it provides a connection between the different properties of the compact objects at the local maximum of the mass for a given branch of solutions.

The study of this universality has been extended in the dissertation to the case of scalar-tensor theories of gravity, furthermore, the addition of non-baryonic EOS has been considered. 53 different EOS candidates have been explored for this purpose and it has been shown that these relations hold for scalarized neutron stars in massive scalar-tensor theories, exploring also the effect of non-baryonic EOS. The obtained relations can be used to explicitly demonstrate that the existing EOS constraints considered in [26] are significantly altered by the GR modifications. The complete results are published in [41].

6.1 Structure equations and methodology

The results have been obtained in a theory with an action in the Einstein frame given by (10). Following [42], an exponential conformal factor $A(\varphi)$ has been used, which is characterized by

a single parameter β, of the form

$$A(\varphi) = e^{\frac{1}{2}\beta\varphi^2}. \tag{73}$$

In addition, the simplest and most natural $\mathbb{Z}_2$ symmetric scalar potential has been used, namely

$$V(\varphi) = 2m_\varphi^2\varphi^2, \tag{74}$$

where m_φ is the mass of the scalar field. This choice of the conformal factor $A(\varphi)$ leads to a STT that is perturbatively equivalent to GR in the weak-field regime but where new effects can appear for strong fields, such as neutron star scalarization that is considered in the present chapter. Note that for this entire section, $\varphi = \varphi(r)$ denotes the scalar field. Even though this same letter is used as an angular coordinate in the original anzatz of the metric (26), the problem has spherical symmetry and so the angular coordinate is not used at all.

Using a standard spherically-symmetric space-time anzatz for the metric (26) and the field equations (11) we get the dimensionally reduced Einstein frame field equations as

$$\frac{2}{r}e^{-2\Lambda}\frac{d\Lambda}{dr} = 8\pi G_* A^4\tilde{\rho} - \frac{1}{r^2}(1-e^{-2\Lambda}) + e^{-2\Lambda}\left(\frac{d\varphi}{dr}\right)^2 + \frac{1}{2}V(\varphi) \tag{75}$$

$$\frac{2}{r}e^{-2\Lambda}\frac{d\Gamma}{dr} = 8\pi G_* A^4\tilde{p} - \frac{1}{r^2}(1-e^{-2\Gamma}) + e^{-2\Lambda}\left(\frac{d\varphi}{dr}\right)^2 - \frac{1}{2}V(\varphi) \tag{76}$$

$$\frac{d\tilde{p}}{dr} = (\tilde{p}+\tilde{\rho})\left(\frac{d\Gamma}{dr} + \frac{d\ln A(\varphi)}{d\varphi}\frac{d\varphi}{dr}\right) \tag{77}$$

$$\frac{d^2\varphi}{dr^2} = \left(\frac{d\Lambda}{dr} - \frac{d\Gamma}{dr} - \frac{2}{r}\right)\frac{d\varphi}{dr} + 4\pi G_* A^4(\varphi)(\tilde{\rho}-3\tilde{p})e^{2\Lambda}\frac{d\ln A(\varphi)}{d\varphi} + \frac{1}{4}\frac{dV(\varphi)}{d\varphi}e^{2\Lambda}. \tag{78}$$

The central values are given in Jordan frame (physical frame) by $\tilde{\rho}(0) = \tilde{\rho}_c$, $\Lambda(0) = 0$ and $\frac{d\varphi}{dr} = 0$. On the other hand, from the asymptotic flatness at infinity we have $\Gamma(\infty) = 0$, $\Lambda(\infty) = 0$ and $\varphi(\infty) = 0$. The central value $\varphi(0) = \varphi_c$ is determined through a shooting method by demanding that the asymptotic value of φ tends to zero. The mass of the scalar field has been taken as $m_\varphi = 10^{-13}$ eV in order to ensure that its Compton wavelength will be much smaller than the orbital distance between the compact objects in the observed binary pulsar systems. The effects from such a small scalar field mass are practically indistinguishable from the massless case, as it can be seen on Fig. 11 (and as it has been shown numerically for all remaining EOS employed in this study).

Numerically, the relative differences in the neutron star masses and the neutron star radii between the cases $m_\varphi = 0$ and $m_\varphi = 10^{-13}$ eV respectively does not exceed 10^{-2} (1%) as obtained for several very different EOSs. The numerical computation of all models have therefore been performed in the massless framework. Indeed, this approximation's validity is supported by the results since the minor corrections to the fits obtained from the mass $m_\varphi = 10^{-13}$ eV are negligible as compared to the obtained fits rms.

Maximum mass universal relations

Lindblom [40] demonstrated that for a wide class of EOS models the $P(\rho)$ dependence in the neutron stars core can be well approximated with only two parameters. Following this idea, Ofengeim showed that within the framework of General Relativity (GR), the sets of points (M_*, R_*, x_{c*}) of maximum-mass neutron stars belong with high accuracy to a single 2-dimensional surface [26] and can be further fitted by analytic expressions. In this notation, M_* and R_* signify the mass and radius at the maximum-mass point of a sequence of neutron star models while $x_* = \tilde{\rho}_{c*}, \tilde{p}_{c*}, \tilde{c}_{sc*}$ takes the values of central density, pressure or speed of sound

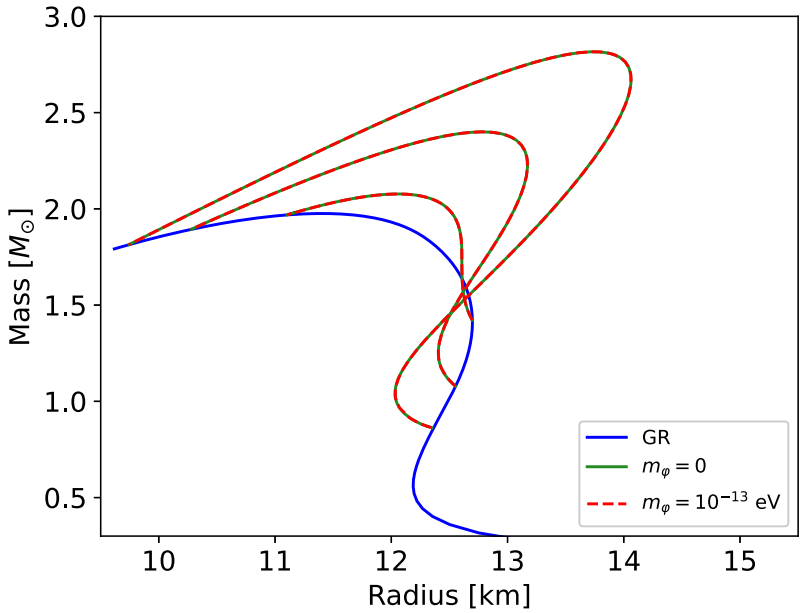

Figure 11: Mass-Radius relations of the ALF2 EOS for GR and $\beta = -5, -6, -7$. Massless and $m_\varphi = 10^{-13}$ eV cases for each β value are shown in solid green and dashed red lines respectively.

for that star. In order to verify this universality and obtain quantitative results of its accuracy, the same fit as in [26] has been used in the dissertation, given by

$$x_* = x_0 \left(\frac{a_x}{R^*_{\mathrm{mix},x} - b_x} \right)^{\mathfrak{p}_x}, \tag{79}$$

where a slight change of notations has been made, using the definition

$$R^*_{\mathrm{mix},x} = R_* \cos\phi_x + r_{g*} \sin\phi_x. \tag{80}$$

The variable ϕ_x has the same interpretation of a mixing angle as indicated by Ofengeim. This angle can be interpreted as the rotational angle between the R_* axis and an approximate line obtained through the projection of the x_*'s cross-section with a horizontal plane. The parameter r_{g*} is simply the star's Schwarzschild radius at the maximum mass point $r_{g*} = 2G_*M_*/c^2$. The four values a_x, ϕ_x, b_x and $\mathfrak{p}_x$ are the fit parameters which are varied in order to minimize (79)'s rms while the values x_0 carry the appropriate dimensionality of pressure, density or speed. This dimensionality has been set by the saturation density of symmetric nuclear matter and naturally – the speed of light. These have been chosen as $\rho_0 = 2.8 \times 10^{14}\ \mathrm{g\,cm^{-3}}$, $P_0 = \rho_0 c^2$ and $c_0 = c$.

Considering $\rho_{c*}(M_*, R_*)$ and $P_{c*}(M_*, R_*)$ as a system of equations, the dependence can be easily inverted. Substituting these results in the fit for c_{sc*}, one can obtain a secondary fit, entirely dependent on the original parameters as

$$y_* = y_0 \left\{ A_y \left[(\rho_0/\tilde{\rho}_{c*})^{1/\mathfrak{p}_{\tilde{\rho}}} \cos\Phi_y + (\rho_0 c^2/\tilde{p}_{c*})^{1/\mathfrak{p}_{\tilde{p}}} \sin\Phi_y - B_y \right] \right\}^{q_y}, \tag{81}$$

where $y_* = M_*, R_*, \tilde{c}_{sc*}$.

One can easily show that $q_{\tilde{p}_{c*}} = q_{\tilde{\rho}_{c*}} = 1$ and $q_{c_{\tilde{s}c*}} = -\mathfrak{p}_{\tilde{c}}$. The remaining parameters are entirely derived from the previous fits with the appropriate normalization condition. An additional mixing variable has also been defined as

$$\chi_{\mathrm{mix},y} = \left(\frac{\tilde{\rho}_0}{\tilde{\rho}_{c*}} \right)^{\frac{1}{\mathfrak{p}_{\tilde{\rho}}}} \cos\Phi_y + \left(\frac{\tilde{\rho}_0 c^2}{\tilde{P}_{c*}} \right)^{\frac{1}{\mathfrak{p}_{\tilde{P}}}} \sin\Phi_y. \tag{82}$$

All of these relations and their fit errors allow us to explore several constraints in the next section, based on causality and the highest measured neutron star masses. Unlike the analogous constraints in GR, these can be interpreted both as EOS and theory constraints based on observational data.

6.2 Results

A a total of 53 EOS including a diverse range of phases and models have been explored in the dissertation. 24 of these are piecewise polytropic approximations based on [8] including SLy, APR1-4, MPA1, MS1-2, MS1b, H1-H7, WFF1-3, ENG and ALF1-4. The remaining 29 are tabulated EOS obtained from the CompStar Online Supernovae Equations of State (CompOSE) [43] including GM1_Y4-6 [44, 45, 46], QHC18-19 [47, 48, 49, 50], SK255, SK272, SKa/b [46, 51, 52, 53], SkI2-6, SkMp, SkOp [46, 53, 54, 55], SLy2,4,9,230a [46, 53, 56, 57, 58] and others [53, 59, 60, 61, 62, 63, 64]. For each of the 53 EOS, a sequence of models have been computed based on adaptive-step Dormand-Prince Algorithm [35] and the maximum mass point of this sequence has been found numerically. The parameters P_{c*}, ρ_{c*}, c_{sc*}, M_* and R_* for GR and five different values of the coupling β from (73) have been found in this way. The fits have been performed by a non-linear least squares method adapted for the particular shape of the functions (79) and (81). The actual sequence of values used is $\beta = \{-5, -5.5, -6, -6.5, -7\}$.

Fig. 12 demonstrates the primary fits (79) obtained with all baryonic EOS for GR and three of the theories with integer β. The complete table of parameters for all fits are available in the dissertation, but only some representative cases have been left on the plot for better readability.

It is apparent from the relative errors that the fit accuracy is at least as good for each of the scalar-tensor theory parameters as it is for GR. The actual rms and maximum deviations for each of the fits can be found in tables in the dissertation. A promising result apparent from the data and the plots, is that the fit parameters are significantly different for the different β values. Although the universality is present for generalized theories, its quantitative aspects are not theory-independent and offer significant distinction between GR and alternative theories on one hand and the parameters of a single theory on the other.

A separate set of fits with all the EOS (including non-baryonic and strong phase transitions) have also been performed and included as numerical values in the dissertation. The fit coefficients for all EOS are very similar, but their root-mean square errors are much larger, which indicates that non-baryonic matter significantly worsens the fits. This is particularly true for the speed of sound in the centre of the neutron stars. For better readability, Fig. 13 shows just one such plot which illustrates this effect for the case $\beta = -6$, where the complete set of EOS are shown with a distinction between the baryonic and non-baryonic EOS. Note that the x-axis $R^*_{\mathrm{mix},x}$ depends on the fit parameters themselves and so we have computed all points' x-value with the same fit coefficients (those for baryons-only).

The following Fig 14 demonstrates the derived secondary fits for the same theories as Fig. 12 for the baryonic-only case, following the form (81) with mixing variable (82). Once again, the relative fit error for GR and the alternative theories is on the same order demonstrating the validity of the universal relations.

The tables containing the full fit parameters in the dissertation show that the baryonic-only secondary fits are once again much better in particular for the speed of sound c_{sc*}. The highest deviation from the fit increases on average 4–5 times after adding the non-baryonic EOS. The same occurs in the GR fits as can be seen on the same tables and so the effect is not caused by the scalar-tensor theory's specifics. For all theories and parameters, QHC18 and QHC19 possess the highest deviation from the fit at nearly 25 % relative difference for the speed of sound. Removing these and the remaining 5 non-baryonic EOS improves the fits significantly, dropping the highest deviation for the central speed of sound to values on the order of 5 %.

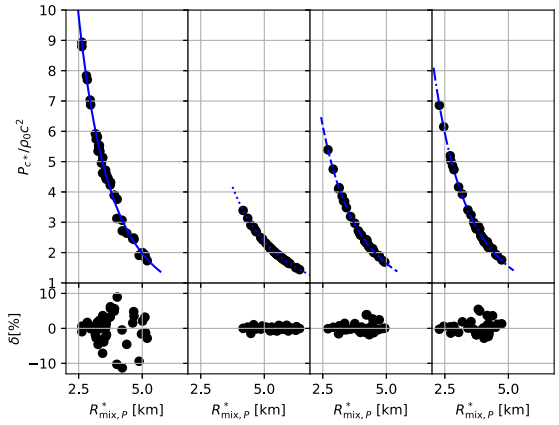

(a) Pressure P_{c*} fits

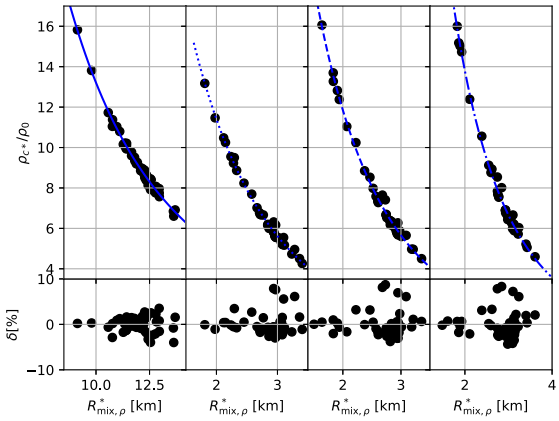

(b) Density ρ_{c*} fits

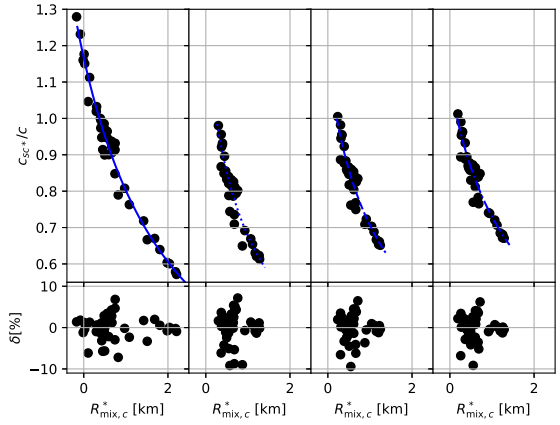

(c) Speed of sound $c_{\mathrm{cs}*}$ fits

Figure 12: $x_*(R^*_{\mathrm{mix},x_*})$ fits of the form (79) going from left to right: GR (solid line), $\beta = -5$ (dotted line), $\beta = -6$ (dashed line) and $\beta = -7$ (dash-dotted line) for the scalar-tensor theory.

While the improvement in the fit of M_* and R_* is not as significant, it is still visible after the removal of non-baryonic EOS. This clearly shows that the universality's accuracy is strongly dependent on the nature of the EOS used. In particular, it shows that even a small amount of non-baryonic EOS with strong phase transitions lead to a large reduction in the fit's accuracy. This reduction in accuracy for a more broad class of EOS does not lead to significant changes in the actual fit parameter values but only their rms and maximum deviation values as seen in the parameter tables included in the dissertation.

After obtaining the values of the fits (79), (81), certain restrictions between neutron star properties or their measured value can be translated into constraints on the EOS. This has been demonstrated in the dissertation for the constraints arising from causality in the centre of the compact object and the highest measured neutron star masses until now. These constraints can be complemented with others based on the maximum possible compactness or constraints derived from binary merger observations.

In the case of causality, the idea is to plot the conditions $c_{sc*}(1 \pm \epsilon_{f,c}) = 1$ where $f = \{MR, P\rho\}$ and so $\epsilon_{f,c}$ corresponds to the relative error in the fits $c_{sc*} = c_{sc*}(M_*, R_*)$ and $c_{sc*} = c_{sc*}(\rho_*, P_*)$ for these two values respectively. Considering the fit definitions (79) and (81), it is easy to show that the condition $c_{sc*} = 1$ corresponds to the region

$$\left(\frac{\rho_0 c^2}{P_{c*}}\right)^{\frac{1}{\mathfrak{p}_P}} + \cot\Phi_c \left(\frac{\rho_0}{\rho_{c*}}\right)^{\frac{1}{\mathfrak{p}_\rho}} = \frac{1}{\sin\Phi_c}\left[B_c + \frac{(1 \pm \epsilon_{P\rho,c})^{-\frac{1}{q_y}}}{A_c}\right] \tag{83}$$

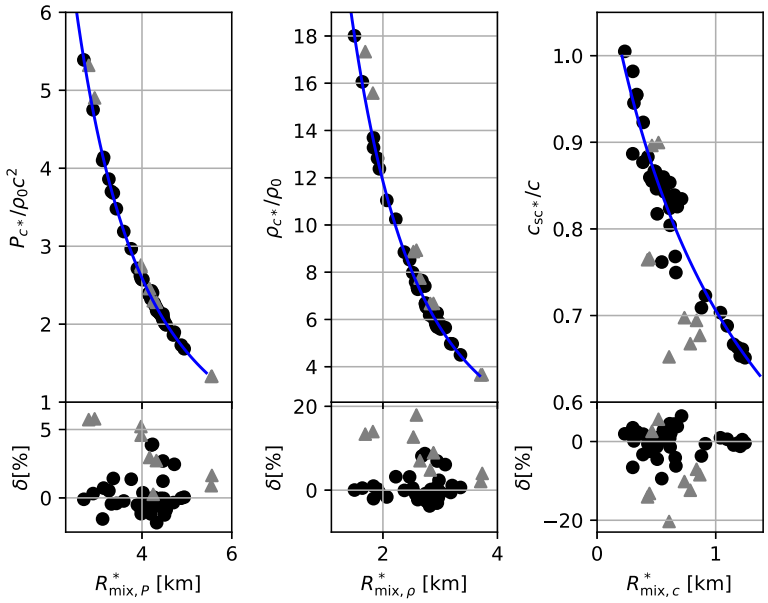

Figure 13: $x_*(R^*_{\mathrm{mix},x_*})$ fits of the form (79) for all EOS at $\beta = -6$. Baryonic points are shown as black circles and non-baryonic points are shown as gray triangles.

in the ρ_{c*}–P_{c*} plane and the region between the two lines

$$M_* + R_* \cot\phi_c = \frac{1}{\sin\phi_c}\left[b_c + a_c(1 \pm \epsilon_{MR,c})^{\frac{1}{\mathfrak{p}_c}}\right] \tag{84}$$

in the M_*–R_* plane.

As far as the maximum mass is concerned – one can apply directly the observational constraint on the maximum static neutron star mass $M_* > 1.97 M_\odot$ to the M_*–R_* plane. In a manner similar to that for the causality, one can also translate this condition in the ρ_{c*}–P_{c*} plane by considering the fit $M_* = M_*(\rho_*, P_*)$ with a given maximum error $\epsilon_{P\rho,M}$. The condition for some fixed mass $M_* = \bar{M} = \text{const}$ is then translated to $M_*(\rho_*, P_*)(1 \pm \epsilon_{P\rho,M}) = \bar{M}$. This is once again easily inverted from (81) as

$$P_{c*} = \left[\frac{1}{\sin\Phi_M}\left(\frac{\bar{M}^{\frac{1}{\mathfrak{q}_M}}}{A_M} + B_M\right) - \left(\frac{\rho_0}{\rho_{c*}}\right)^{\frac{1}{\mathfrak{p}_\rho}} \cot\Phi_M\right]^{-\mathfrak{p}_P}. \tag{85}$$

All restrictions resulting from each of the 6 theories with different β have been obtained in both the Mass-Radius and Density-Pressure planes. The effects obtained for GR and $\beta = -5$ are shown on Fig. 15 It becomes apparent from the expressions that larger fit error leads to significant loosening of the restrictions posed by the two conditions (i.e. more EOS are allowed). Indeed, the fits containing just 7 non-baryonic EOS fail to provide significant restrictions even in the GR case and so we have used the more severe restrictions posed by the baryonic-only fits similar to [26].

6.3 Commentary

A known obstacle in the study of modified theories of gravity through neutron stars has been the ambiguity in the Equation of State (EOS) governing their internal structure. While the EOS for nuclear matter bellow the saturation density is well known, the central regions of neutron stars reach higher densities under which the exact state of matter is not yet well understood.

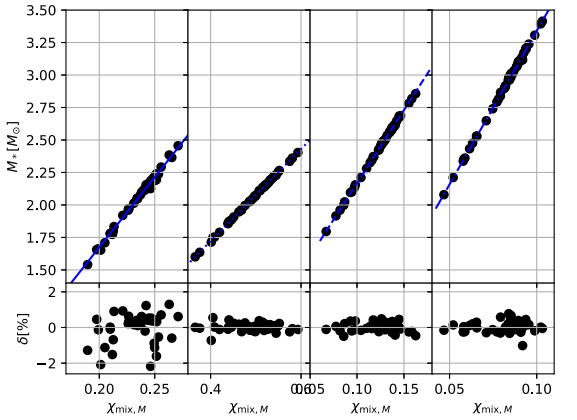

(a) Mass M_* fits

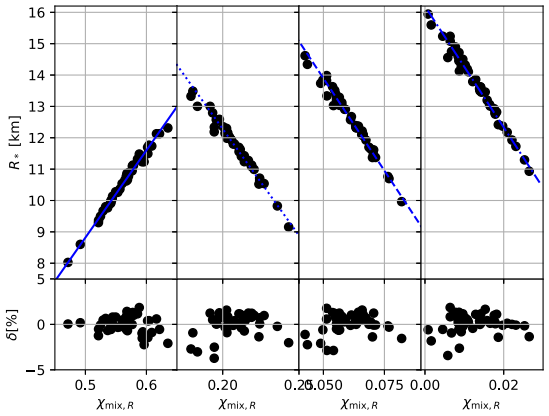

(b) Radius R_* fits

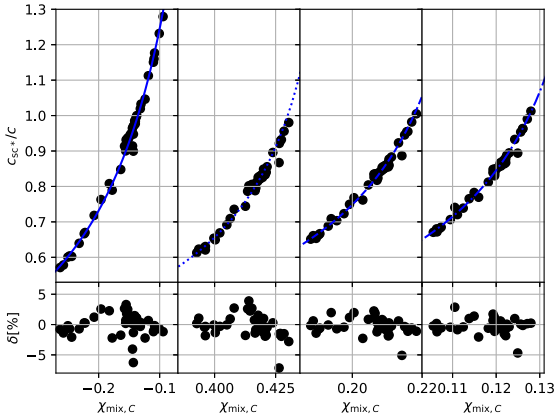

(c) Speed of sound $c_{\mathrm{cs}*}$ fits

Figure 14: $y_*(\chi_{\mathrm{mix},y_*})$ fits of the form (81) going from left to right: GR (solid line), $\beta = -5$ (dotted line), $\beta = -6$ (dashed line) and $\beta = -7$ (dash-dotted line) for the scalar-tensor theory.

A novel type of universality (EOS independence) relations connecting the neutron stars properties at the maximum-mass points for neutron star sequences in a certain class of massive scalar-tensor theories (STT) have been confirmed to hold in the dissertation. More importantly, it was discovered that the fit parameters of these universal relations vary significantly with the ST theory and its parameters. The general effect of the scalar-tensor theory can be broken down intuitively in two components. First of all, the scalar field provides additional internal energy support against collapse which is proportional to the value of β and supports higher values of the maximum mass with the increase of this parameter. The second consequence of this is that the maximum-mass point is reached at lower pressure values for higher β values. Therefore, even equations of state which violate causality in GR are reconciled with the constraint as early as $\beta = -5$. Indeed, for values of $\beta < -6$ all considered EOS fit within the obtained constraints.

In addition to the exploration of these universal relations outside of GR, the behavior of the fits under the addition of non-baryonic EOS were studied for the first time, confirming that even with the addition of a small number of these, rms and maximum deviations of the fits are significantly worsened. In order to keep the results unbiased, a total of 53 equations of state have been used, including both polytropic approximations and tabulated versions of different high-density matter leading to a wide array of physical and even non-physical (from causality perspective) maximum mass states. Importantly, it has been verified that the introduction of non-baryonic EOSs degrades the fit quality without changing the actual values for the fit

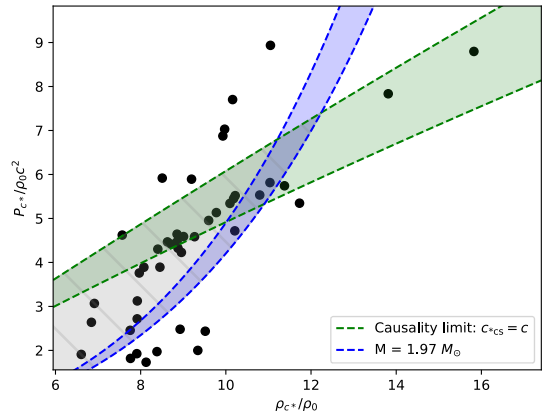

(a) GR restrictions in $P(\rho)$ plane

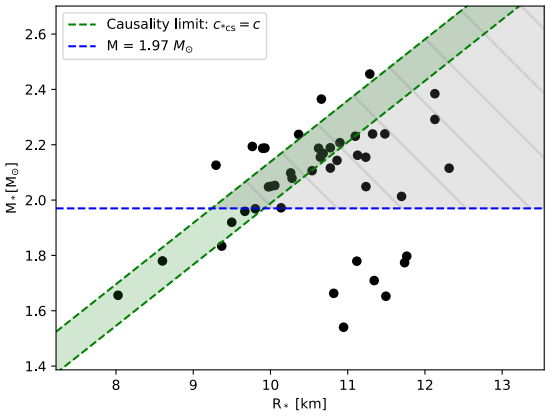

(b) GR restrictions in $M(R)$ plane

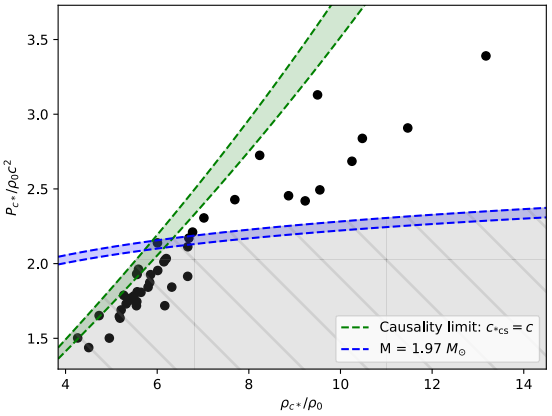

(c) $\beta = -5$ restrictions in $P(\rho)$ plane

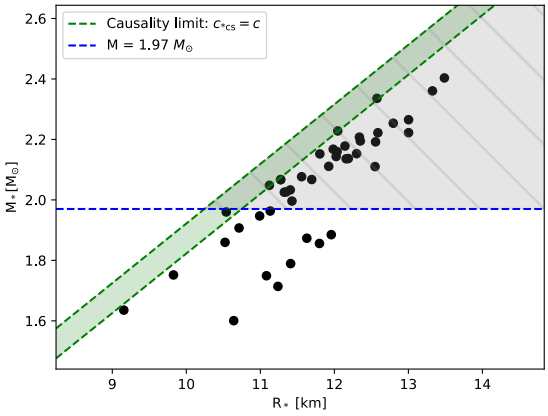

(d) $\beta = -5$ restrictions in $M(R)$ plane

Figure 15: Final constraints on Mass-Radius and Pressure-Density using only baryonic EOS for GR and $\beta = -5$ STT. The region in gray shows the region which agrees with the measured maximum mass and causality, the remaining regions are constrained.

parameters significantly. On the other hand, STTs lead to significantly different universal relation fit parameters compared to GR that are outside of the rms deviations even if non-baryonic EOS are taken into account.

Lastly, constraints on the allowed EOS in the Mass-Radius and Pressure-Density planes were derived based on observations and physical causality with the aid of the obtained universal relations. In most cases, though, the universal relations of baryonic-only matter can produce good enough restrictions due to the larger spread present with the introduction of non-baryonic EOS. This methodology can be used in the following ways:

- Assuming that a given gravitational theory is correct, the universal relations can be used to constrain the physical EOS based on different observations and theoretical limits, e.g. the NS maximum mass and causality. This is important since currently most of the observations are interpreted with the assumption that GR is the correct theory which can cause difficulty when testing the strong field regime of gravity.

- Assuming that the equation of state (EOS) is further constraint by the experiments, the relations can be used to constrain the allowed range of β parameters for the considered class of STT. The novel experiments of heavy ion collisions promise to allow for such application within the coming decade.

- If further independent constraints on the NS properties are obtained in the future, e.g. by the gravitational wave and electromagnetic observations, their simultaneous application can constrain the theory of gravity in an EOS independent way (e.g. it may turn out that these constraints are incompatible for certain value of the STT parameters).

In other words, it may turn out that this kind of constraints do not permit entire regions of the parameter to lead to physically-meaningful solutions for entire EOS, but constrain EOS for other regions of the parameter.

7 Constraining Gauss-Bonnet scalarization through binary pulsars

Strong constraints of Gauss-Bonnet theories of gravity imposed by neutron star – white dwarf (NS-WD) binary system observations have been explored in the dissertation. More specifically, this has been achieved by comparing the orbital period evolution due to the emission of gravitational radiation in well chosen NS-WD pairs for different theory parameters through Bayesian analysis. The actual inference is performed through Markov Chain Monte Carlo (MCMC) method, sampling the parameters of the theory and the central pressure of the Neutron Star (NS) models and comparing with the observations to form a posterior probability function.

Even though scalarization in sGB gravity originally attracted a lot of attention in the context of black holes, it is also possible to scalarize neutron stars [65, 66, 67]. This is important because even though scalarization in sGB gravity brought a lot of excitement, little is known about the astrophysical implications and the theory has not been strongly constrained previously. The observations are based on the most suitable pulsar – white dwarf binaries which have been used to constrain the DEF model [68]. The complete results are published in [69].

7.1 Structure equations and methodology

The results have been obtained within the framework of the scalar Gauss-Bonnet (sGB) theory described in 2.3 through the analysis of static neutron stars described by the metric (26). The matter source is taken as perfect fluid (22) as described in section 3.2. Using this anzatz and translating the staticity and spherical symmetry to the fluid and the scalar field, the field equations (15) and (16) lead to the reduced form

$$\frac{2}{r}\left[1+\frac{2}{r}(1-3e^{-2\Lambda})\Psi_r\right]\frac{d\Lambda}{dr}+\frac{(e^{2\Lambda}-1)}{r^2}-\frac{4}{r^2}(1-e^{-2\Lambda})\frac{d\Psi_r}{dr}-\left(\frac{d\varphi}{dr}\right)^2=8\pi G_*\rho e^{2\Lambda}, \tag{86}$$

$$\frac{2}{r}\left[1+\frac{2}{r}(1-3e^{-2\Lambda})\Psi_r\right]\frac{d\Gamma}{dr}-\frac{(e^{2\Lambda}-1)}{r^2}-\left(\frac{d\varphi}{dr}\right)^2=8\pi G_* P e^{2\Lambda}, \tag{87}$$

$$\frac{d^2\Gamma}{dr^2}+\left(\frac{d\Gamma}{dr}+\frac{1}{r}\right)\left(\frac{d\Gamma}{dr}-\frac{d\Lambda}{dr}\right)+\frac{4e^{-2\Lambda}}{r}\left[3\frac{d\Gamma}{dr}\frac{d\Lambda}{dr}-\frac{d^2\Gamma}{dr^2}-\left(\frac{d\Gamma}{dr}\right)^2\right]\Psi_r-\frac{4e^{-2\Lambda}}{r}\frac{d\Gamma}{dr}\frac{d\Psi_r}{dr}+\left(\frac{d\varphi}{dr}\right)^2=8\pi G_* P e^{2\Lambda}, \tag{88}$$

$$\frac{d^2\varphi}{dr^2}+\left(\frac{d\Gamma}{dr}-\frac{d\Lambda}{dr}+\frac{2}{r}\right)\frac{d\varphi}{dr}-\frac{2\lambda^2}{r^2}\frac{df(\varphi)}{d\Gamma}\left\{(1-e^{-2\Lambda})\left[\frac{d^2\Gamma}{dr^2}+\frac{d\Gamma}{dr}\left(\frac{d\Gamma}{dr}-\frac{d\Lambda}{dr}\right)\right]+2e^{-2\Lambda}\frac{d\Gamma}{dr}\frac{d\Lambda}{dr}\right\}=0, \tag{89}$$

where from eq. (18) we have

$$\Psi_r = \lambda^2 \frac{df(\varphi)}{d\varphi}\frac{d\varphi}{dr}. \tag{90}$$

Additionally, the hydrostatic equilibrium equation takes the form

$$\frac{dP}{dr} = -(\rho + P)\frac{d\Gamma}{dr}, \tag{91}$$

which follows from (19) applied for a perfect fluid. Note that for this entire section, $\varphi = \varphi(r)$ denotes the scalar field. Even though this same letter is used as an angular coordinate in the original anzatz of the metric (26), the problem has spherical symmetry and so the angular coordinate is not used at all.

The regularity at the center and asymptotic flatness impose the following boundary conditions

$$\Lambda|_{r\to 0} \to 0, \quad \left.\frac{d\Gamma}{dr}\right|_{r\to 0} \to 0, \quad \left.\frac{d\varphi}{dr}\right|_{r\to 0} \to 0 \ , \tag{92}$$

$$\Lambda|_{r\to\infty} \to 0, \quad \Gamma|_{r\to\infty} \to 0, \quad \varphi|_{r\to\infty} \to 0 \ . \tag{93}$$

The leading order asymptotic of the scalar field at infinity has the form

$$\varphi \approx \frac{D}{r} + O\left(\frac{1}{r^2}\right). \tag{94}$$

where the scalar charge D is a constant directly related to the gravitational wave emission in close binary systems, entering in equation (60) applied in the sGB theory case.

The existence and stability of scalarized neutron star solutions has been studied in [66]. For the purpose of this exploraton, equations (86)–(89) have been considered with the following commonly used coupling function

$$f(\varphi) = \frac{\epsilon}{2\beta}[1 - \exp(-\beta\varphi^2)] \tag{95}$$

where $\beta > 0$ and $\epsilon = \pm 1$. While for both $\epsilon = \pm 1$ scalarized neutron stars solutions exist, static black holes can only scalarize for positive ϵ [70]. The minus sign of ϵ is associated with the so-called spin-induced scalarization [71, 72] where the development of scalar field is observed only for sufficiently rapidly rotating neutron stars. In order to obtain neutron star solutions for different β and λ values corresponding to one of the partners in a neutron star–white dwarf (NS–WD) binary system the methodology described in [66] has been followed closely. As already shown in [66], the considered theory approaches standard GR as β tends to infinity. Therefore, to avoid a growing probability function for larger values in the parameters space, we have reparametrized (95) by the inverse parameter $\kappa \equiv \beta^{-1}$ for all numerical computations.

The coupling function choice (95) is by no means unique, but it has been chosen due to the stability of both neutron stars and black holes within a theory considering it, which allows us to translate the obtained constraints to the latter. Moreover, as the experience from other studies shows [73, 74], if we consider a modified coupling that still leads to well-behaved branches of solutions, the final results will remain qualitatively the same.

The investigation has been focused on state-of-the-art observations of a set of three neutron star-white dwarf (NS-WD) binaries listed in Table 1, following the MCMC strategy as formulated by [68], in order to derive constraints in the κ – λ space. These pairs are J0348+0432, J1012+5307 and J2222–0137, and the numerical values of the parameters for each system are

available in the table. It should be noted that the considered binary pulsars are rotating with a spin frequency within the range 30-200 Hz. This is still well within the slow rotation regime where the static spherically symmetric solutions are a very good approximation. This is especially true for the stellar mass and scalar charge where the rotational corrections are already of second order with respect to the spin and would not lead to more than 3 % correction with respect to the static case. For this reason, static spherically symmetric scalarized neutron stars have been considered as a good approximation to the observed pulsars, similar to the approach in [68] used for constraining the DEF model.

Quantity	J0348+0432 values	J1012+5307 values	J2222–0137 values
Orbital Period (P_b) in days	$0.102424062722 \pm 7 \times 10^{-12}$	$0.60467271355 \pm 3 \times 10^{-11}$	$2.445759995471 \pm 6 \times 10^{-12}$
Eccentricity (e)	$2.6 \times 10^{-6} \pm 9 \times 10^{-7}$	$1.2 \times 10^{-6} \pm 3 \times 10^{-7}$	$3.8092 \times 10^{-4} \pm 4 \times 10^{-8}$
Intrinsic $\dot{P}_b^{\rm int}$ in (fs.s^{-1})	-274 ± 45	-2.1 ± 8.6	-10 ± 8
NS to WD mass ratio $q \equiv m_p/m_c$	11.70 ± 0.13	10.44 ± 0.11	n/a
Pulsar mass $m_p^{\rm obs}$ in $M_\odot$	$*2.0065^{+0.0755}_{-0.0570}$	$*1.72^{+0.18}_{-0.17}$	1.81 ± 0.03
Observed WD mass $m_c^{\rm obs}$ in $M_\odot$	$0.1715^{+0.0045}_{-0.0030}$	0.165 ± 0.015	1.312 ± 0.009

Table 1: Physical parameters for the NS–WD pairs used for the inference of constraints. Values are obtained from [75, 76, 77, 78, 79] where the observed time derivatives are corrected using the Galactic potential of [80]. Values marked with * are not directly observed but derived from the remaining measurements.

Within the dissertation, it is shown that the more massive a pulsar is, the better its constraints on the theory are. The binaries from Table 1 have been chosen specifically due to the precision of their orbital period change and the object masses. Even though there's a binary with a more massive pulsar discovered, namely J0740+6620 [81], this system does not yet have a well-measured $\dot{P}_b$ which does not permit it to be used for a constraint. As seen in [66], for greater λ, the bifurcation point from the GR branch will appear at lower masses. Therefore, less massive neutron stars will generally provide constraints starting from larger λ values and will not contribute to a distribution where constraints from more massive stars are considered. This will be seen in the numerical results for these three NS–WD pairs in 7.2. Since J0348+0432 is currently the most massive pulsar with a well measured orbital decay, it provides the best constraints. The same methodology can be readily applied to future NS–WD pairs with higher pulsar mass and well measured orbital decay but, given that the maximum neutron star mass is close to two solar masses, it is expected that other pulsars can improve the constraints only slightly.

We follow Bayes' theorem for the purposes of the analysis with posterior distribution variables $\vec{\zeta} \equiv (\kappa, \lambda)$. The hypothesis $\mathcal{H}$ in our case is the sGB gravity for certain κ and λ values. During an MCMC run, all remaining parameters are integrated over to obtain the marginalized posterior distribution in terms of just (κ, λ). For a given NS–WD system, the gravitational dipole radiation can be described by 3 free parameters, namely the theory parameters (κ, λ) and the central pressure P_c or central density ρ_c of the pulsar, provided that all other orbital details such as the eccentricity, orbital period, etc. are well measured. The central value of the scalar field φ_c on the other hand is obtained through a shooting method from the requirement that the scalar field is zero at infinity $\varphi_\infty = 0$.

The MCMC runs evolve the 3 parameters through an affine-invariant ensemble sampler available with the Python `emcee` package [37, 33] as described in Section 4. The prior distribution is homogeneous in areas of the (κ, λ) space where scalarized solutions exist. P_c is also sampled homogeneously, but in the range of pressure values which would produce the observed pulsar mass of the system, considering its error bounds. The dimensionally reduced field equations (86) – (89) are solved at each step. The likelihood function is then computed by comparing the observed decay of the binary system's orbital period with that predicted for

the sGB theory considering the given parameters from the simulations. Following [68], the logarithmic likelihood is defined as

$$\ln \mathcal{L} \propto -\frac{1}{2}\left[\left(\frac{\dot{P}_b^{\rm int}-\dot{P}_b^{\rm th}}{\sigma_{\dot{P}_b}^{\rm obs}}\right)^2+\left(\frac{m_p/m_c-q}{\sigma_q^{\rm obs}}\right)^2\right], \tag{96}$$

where m_p and m_c are the pulsar and companion masses of the system, q is the observed mass ratio, $\dot{P}_b^{\rm int}$ is the observed intrinsic orbital period decay rate, $\dot{P}_b^{\rm th}$ is the predicted one and $\sigma_X^{\rm obs}$ is the uncertainty from observations for the respective quantity X. The second term in (96) is adapted based on whether the ratio q and the WD mass m_c or both masses are known as per Table 1. The predicted orbital decay is dominated by the dipole scalar and quadrupole tensor radiation terms which are adapted from (60) and (58) respectively, modifying the dipole term for sGB gravity as follows

$$\dot{P}_b^{\rm dipole} \;=\; -\frac{2\pi G_*}{c^3}g(e)\left(\frac{2\pi}{P_b}\right)\frac{m_p m_c}{m_p+m_c}\left(\frac{D}{m_p}\right)^2, \tag{97}$$

while the functions $g(e)$ and $f(e)$ keep their definitions as per (61) and (59). In addition, the bare gravitational constant G_* is used in (58) in the case of GB theory. The quantities in (97) keep the same meaning as those in (60), adding only the dipole charge D evaluated in solar masses. Therefore, for the purpose of the simulation, the period decay is computed as $\dot{P}_b^{\rm th}=\dot{P}_b^{\rm dipole}+\dot{P}_b^{\rm quad}$ using the right hand quantities from (97) and (58).

7.2 Results

All numerical simulations are performed with the coupling functions (95) using $\kappa=\beta^{-1}$ as a dimensionless free parameter for both signs of ϵ. All results are presented in terms of the dimensionless theory parameter defined as

$$\lambda \to \frac{\lambda}{R_0}, \tag{98}$$

where $R_0 \cong 1.4766$ km corresponds to half the Schwarzschild radius of an object with 1 solar mass. The numerical integration of the equations for each MCMC step is performed through an adaptive step method based on the Dormand–Prince version [35] and shooting method for the φ_c and Γ_c values, after which the mass and scalar charge are extracted from the solution's asymptotics. As was already explored in [66], the shooting procedure for the scalar field is not always easy to converge and some manual work was required to choose appropriate initial guesses for the explored regions of (κ,λ).

For each of the runs, a total of 416000 points have been used for the `emcee` sampler in a parallel run. These do not include an initial "shakedown" run of 41600 points used to forget the initial conditions which have been originally chosen uniformly around the prior distribution range. The `emcee` sampler was run with 32 samplers, meaning that these points are split at 1300 shakedown and 13000 run points per random walker making use of parallel computation with the maximum available machine threads. Since the $\epsilon=1$ case turns out to be more difficult numerically (as will be discussed in section 7.2), we have used twice as many points for obtaining the results there. While this number did not significantly influence the derived constraints on the theory parameters) (less than 1% variation), it improved the quality of the plots significantly.

Since there are no obvious limits to the theory parameters (κ,λ), different priors were attempted in order to check the sensitivity of the final constraints on their ranges. The limit $\kappa \to 0$ translates to $\beta \to \infty$ which corresponds to GR with a zero scalar field. As it turns out,

approaching this point leads to undesired numerical problems since we have to be able to calculate scalarized neutron star solutions with almost vanishing scalar field close to the numerical error. Furthermore, obtaining scalarized solutions in the large κ range is also computationally difficult since the scalarized branches become increasingly short in this case [66] and thus solutions exist only very close to the bifurcation point. As shown by the results presented further down, this is purely a numerical problem and GB stars are present for arbitrarily large values of κ. Due to these limitation, however, we had to introduce a cutoff of κ at both large and small value. The choice of these constraints was made in such a way that the final constrains change by at most 2% when decreasing/increasing the lower/upped κ limit twice. This cutoff error is much smaller compared to the difference due to different pulsars and EOS.

On the other hand, the λ range which provides physically meaningful solutions is highly dependent on the neutron star maximum mass and thus the EOS. For a given fixed neutron star mass m_p, decreasing λ for a particular EOS will lead to a critical point $\lambda_{\rm bif}(m_p)$ for which the bifurcation point from the GR branch is exactly at that NS mass m_p. This value is also dependent on the EOS as it has been shown and is therefore an important parameter to know for each run since for $\lambda < \lambda_{\rm bif}$ the scalarized GB branch does not yet exist and thus the scalar dipole radiation contribution is zero.

Results for $\epsilon = -1$

The results of each MCMC run have been analyzed and visualized in two different ways: as scatter plots of the sampled points in the free parameters space and as corner plots showing cumulative probability intervals. The following Fig.16 is an example of these two visualizations for the same run of the MPA1 equation of state (EOS) with the J0348+0432 data and $\epsilon = -1$.

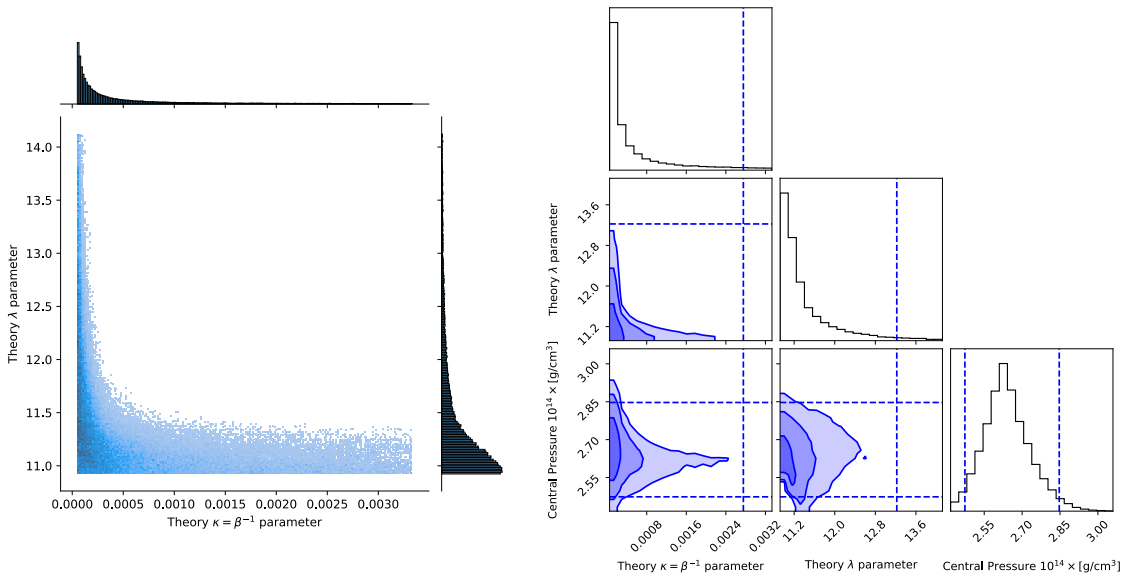

(a) Scatter Plot (b) Corner Plot

Figure 16: Comparison of the scatter and corner plots for the MPA1 EOS with the J0348+0432 NS–WD pair and $\epsilon = -1$. The scatter plot shows directly the density of samples in the theory parameters space while the corner plot shows the quantiles for 95%, 80% and 65% cumulative probability in the different possible 2D cross-sections. The marginalized 1D distributions for each of the quantities are shown on both subplots as histograms

The most straightforward way to compare different constraints would be to compare their quantiles. For all EOS and NS–WD pairs analysed, the distributions are very similar in shape

NS–WD Pair	$\lambda_{\rm bif}$	λ 95% quantile
J0348+0432	10.92	13.22
J1012+5307	13.33	14.59
J2222–0137	12.47	14.12

Table 2: Results for the bifurcation line ($\lambda_{\rm bif}$) and the 95% one-sided quantile interval for the three pulsars with the MPA1 Equation of State and $\epsilon = -1$.

and have several common characteristics. In all cases the central pressure distribution has a maximum very close to the central pressure for the given pulsar mass and EOS in General Relativity, as expected. Furthermore, in all cases the κ and λ marginalized distributions have similar shapes, decreasing rapidly with higher κ and λ values and with maximums around $\kappa = 0$ and $\lambda = \lambda_{\rm bif}$ respectively. The shape of the κ distribution is intuitively explained when we note that for lower κ the solutions tend closer to GR for an increased interval of λ values, making the GB theory indistinguishable from GR in the whole λ interval considered for $\kappa < 10^{-4}$. Indeed, the primary difference between the distributions is the location where the solutions appear ($\lambda_{\rm bif}$, bellow which we cannot make any inference) and the upper boundary of the λ values for the considered range. Therefore, we have adopted $\lambda_{\rm bif}$ and the 95% one-sided quantile interval for λ as our quantitative constraints for each EOS and each system.

Results for different NS–WD at $\epsilon = -1$

Table 2 summarizes the results for MPA1 with the three different pulsars for $\epsilon = -1$. It is sufficient to demonstrate that the most stringent constraints will arise from the most massive pulsar.

Fig. 17 shows the scatter density plot for the MPA1 equation of state based on the above discussion for all 3 NS–WD pairs from Table 1. For each binary system the dashed line represents the scalarization threshold $\lambda_{\rm bif}$ while the scatter of points above it reflects the probability density from the MCMC sampler where scalarized neutron stars exist and their scalar radiation is within the observational bounds for the pulsar. In the region bellow the dashed line scalarization for this pulsar mass is not possible and thus it is by default allowed by the observations of the corresponding binary system. These have not been colored in order to avoid too many overlaps. On the right, a marginalized distribution for each of the pulsars can be seen (integrated over κ).

As it can be seen, the three double systems do not complement each-other significantly since the ranges of viable constraints have very small overlaps. While J2222-0137 and J1012+5307 can provide constraints on the parameter space only for $\lambda > 12.5$, J0348+0432 puts that region at a negligible probability relative to the region $\lambda < 12$.

In fact, Fig. 17 shows that the most stringent constraints from all NS–WD pairs will come from the most massive pulsar J0348+0432 and will not be further constrained even from the inclusion of the remaining two intermediate mass NS-WD binary in Table 1. This is the rationale behind presenting results only for a limited number of NS-WD pairs, even though initially more pairs from the list in [82] were considered. We will continue only with the system which has the most massive pulsar J0348+0432 when computing constraints for multiple different EOS.

The only presently known NS–WD pair which could feasibly provide further constraint is the system J0740+6620 which was already mentioned. Based on the NS parameters measured in [81], the bifurcation point for it is at $\lambda_{\rm bif} = 10.26$. Once measurements of $\dot{P}_b$ are available, this pair can indeed improve the present constraint by approximately 5%. Taking into account, though, that the present observations support the hypothesis that the neutron star maximum mass is not much higher than two solar masses, one can not expect significant improvement

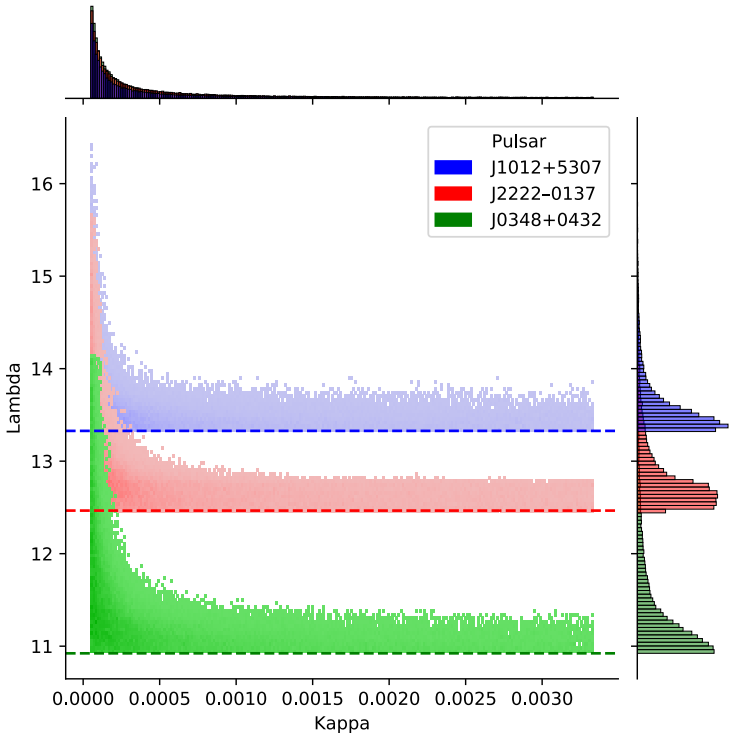

Figure 17: Comparison of the bifurcation point λ_{bif} (dashed lines) and the MCMC samples scatter results for the three pulsars listed in Table 1 and the MPA1 equation of state. The colored region for each binary system is where scalarized neutron stars exist and their scalar radiation is within the observational bounds for the given system. The region bellow the dashed line for each system has no constraints for the given NS–WD pair as it is bellow the bifurcation point, i.e. there scalarization for this pulsar mass is not possible and thus the scalar gravitational radiation is zero. Thus, even though this is also a region allowed by observation it has not been colored to avoid too many overlaps.

beyond this.

Results for different EOS at $\epsilon = -1$

Having demonstrated that the most massive pulsar J0348+0432 gives the strongest constraints, the dissertation addresses the question of how sensitive these constraints are to the nuclear matter EOS. Table 3 provides data for the same quantitative constraints with 10 different EOS based on multi-polytrope approximations from [8]. These include MPA1, APR3, APR4, ENG, H4, SLy, WFF1, WFF2, MS1 and MS1b EOS The rest of the EOS in [8] have not been used due to their low maximum masses which do not support the existence of a pulsar such as that found in J0348+0432 and are therefore considered obsolete.

The following Fig. 18 outlines the boundaries obtained at the bifurcation point $\lambda = \lambda_{\text{bif}}$ (dashed line) and the MCMC samples scatter results for eight of these equations of state. Only data for the J0348+0432 system is plotted as it provides the most stringent constraints. MS1 and MS1b EOS have been excluded from the plot for better visibility since they provide very loose constraints with $\lambda_{\text{bif}} > 15$.

It is once again quite evident that except for a few EOS, the domains of mutual constraints are quite limited. The most stringent limitations on the parameters come from SLy and WFF1 with the rest of the EOS providing virtually no additional constraint on top of them. It is important to note that the regions in λ-space where probability is non-negligible above the bifurcation point are quite similar for all EOS (as can also be seen in Table 3). It is therefore

EOS	$\lambda_{\rm bif}$	λ 95% quantile
MS1	16.02	17.94
MS1b	15.79	17.73
MPA1	10.92	13.22
APR3	9.63	11.98
ENG	8.72	11.11
H4	8.60	10.83
APR4	7.67	9.99
WFF2	7.38	9.94
SLy	6.78	9.40
WFF1	6.34	8.93

Table 3: Results for the bifurcation line ($\lambda_{\rm bif}$) and the 95% one-sided quantile interval for the 10 different EOS used with the J0348+0432 NS–WD pair and $\epsilon = -1$.

evident that the primary factor for the constraints on the (λ, κ) space is when the bifurcation from GR occurs. The appearance of this bifurcation, however, has not been directly traced to a EOS trait which can be quantified. The only observation we have made is that the higher maximum mass EOS, such as MPA1 and APR3 normally lead to weaker constraint. Taking into account the current EOS constraints, as well as the fact that a given EOS should reach the two solar mass barrier, one can safely claim that the constraints shown in Fig. 18 for the WFF1 EOS can not be significantly improved for another realistic EOS.

Results for $\epsilon = 1$

Unlike the $\epsilon = -1$ case, solutions for the $\epsilon = 1$ coupling function with observationally significant values for the scalar charge are much harder to find in a wide range of the free parameters. As will be shown on the plots further down, the intervals of allowed scalarized solutions above the bifurcation point $\lambda_{\rm bif}$ are much smaller. The reason is that the dipole radiation term for this sign of the coupling function grows to values far exceeding those consistent with the observations at just under 4% above the bifurcation point $\lambda_{\rm bif}$ for all explored cases. The reason is that the dipole radiation term for this sign of the coupling function grows to values far exceeding those consistent with the observations at just under 4% above the bifurcation point $\lambda_{\rm bif}$ for all explored cases.

The results of the MCMC runs for $\epsilon = 1$ have been again analyzed and visualized in two different ways: as scatter and corner plots. The results for the MPA1 EOS with the J0348+0432 data are presented in Fig.19 to make a parallel to Fig.16. It is apparent that the scatter of allowed λ values is much smaller and the 95% one-sided quantile interval is very close to the $\lambda_{\rm bif}$ line (only about 4% above it).

Considering the computationally more difficult problem of finding solutions for the $\epsilon = 1$ coupling function, we have explored only selected EOS with the J0348+0432 NS–WD pair for it. The results for the three most relevant equations of state are provided in Table 4 in the same format as that from Table 3.

Fig. 20 outlines the boundaries obtained at the bifurcation point $\lambda = \lambda_{\rm bif}$ (dashed line) and the scatter plots resulting from the MCMC runs for the same three EOS, once again using only data for the J0348+0432 system which provides the most stringent constraints. As evident from the figure's marginalized plots on the right, regions of allowed values are much smaller than the $\epsilon = -1$ case in Fig. 18. The reason for this, as explained above, is that after the bifurcation point the neutron star solutions with $\epsilon = 1$ start developing scalar charge much more rapidly compared to their counterparts for $\epsilon = -1$, thus leading to strong scalar dipole radiation that

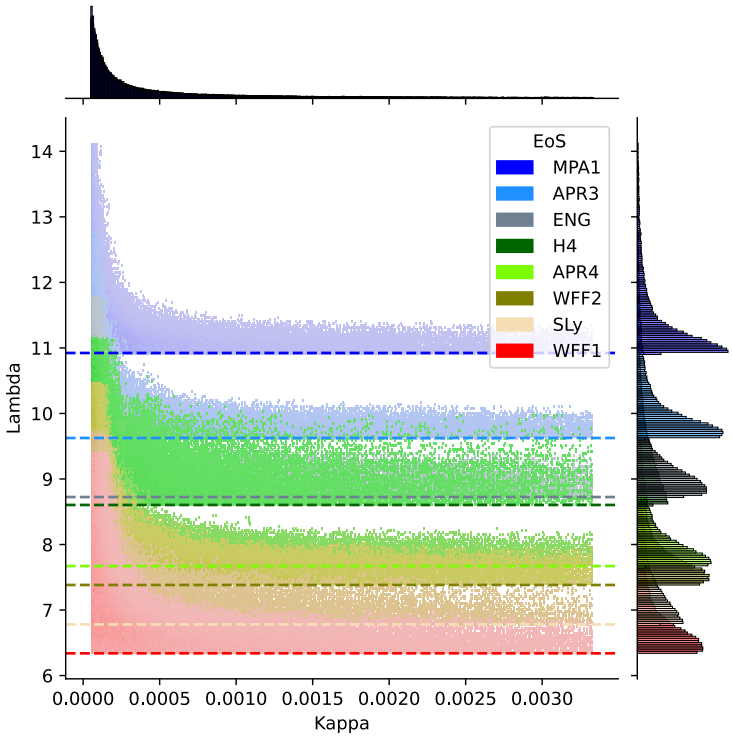

Figure 18: Comparison of the bifurcation point $\lambda_{\rm bif}$ (dashed line) and the MCMC samples scatter results for J0348+0432 with eight realistic nuclear EOS. The colored region for each EOS is where scalarized neutron stars exist and their scalar radiation is within the observational bounds for the system. The region bellow the dashed line for each EOS has no constraints for the given NS–WD pair as it is bellow the bifurcation point, i.e. there scalarization for this pulsar mass is not possible and thus the scalar gravitational radiation is zero. Thus, even though this is also a region allowed by observation it has not been colored to avoid too many overlaps.

is excluded from the observations. Therefore, in this case the observational constraint comes from the $\lambda = \lambda_{\rm bif}$ line directly, since even slightly larger values of λ break the observational constraints.

As can be inferred from Table 4, the values of $\lambda_{\rm bif}$ and the 95% one-sided quantile interval for λ are within 4% of each-other. This shows that the $\epsilon = 1$ case is in fact characterized almost completely by the bifurcation point and there is virtually no possibility for different EOS to complement each-other in constraining the theory parameters. On the other hand, the much higher numerical values for $\lambda_{\rm bif}$ show that this coupling function is less constraining in terms of the GB theory parameter.

EOS	$\lambda_{\rm bif}$	λ 95% quantile
MS1	34.51	35.35
MPA1	23.98	24.51
WFF1	14.78	15.51

Table 4: Results for the bifurcation line ($\lambda_{\rm bif}$) and the 95% one-sided quantile for the 3 representative EOS used with the J0348+0432 NS–WD pair and $\epsilon = 1$.

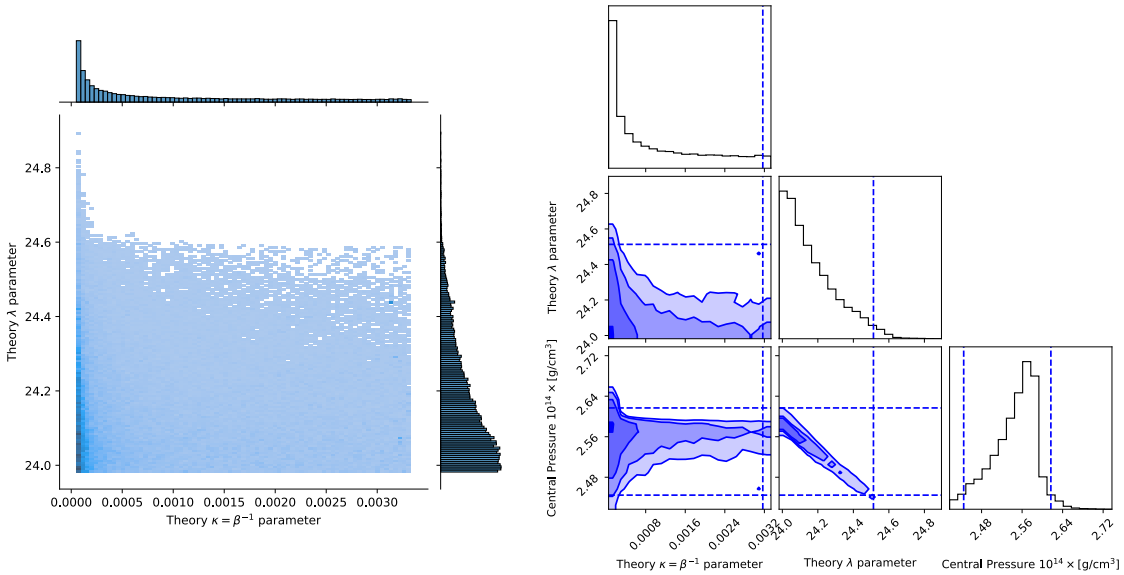

(a) Contour Plot (b) Corner Plot

Figure 19: Comparison of the scatter and corner plots for the MPA1 EOS with the J0348+0432 NS–WD pair and $\epsilon = 1$. The scatter plot shows directly the density of samples in the theory parameters space while the corner plot shows the quantiles for 95%, 80% and 65% cumulative probability in the different possible 2D cross-sections. The marginalized 1D distributions for each of the quantities are shown on both subplots as histograms.

Constraining black hole scalarization with $\epsilon = 1$

In order to apply the obtained constraints to scalarized black holes, we have once again reverted to the parameter β from (95) as the more standard one. For fixed λ and β, though, a whole branch of scalarized black holes can exist with masses from the bifurcation point all the way to negligible (zero) black hole mass. We have decided to focus on two characteristics features of these branches: the black hole mass at the point of bifurcation that represents the maximum mass of a scalarized black holes and depends only on λ, and the maximum scalar charge that can be reached for the whole sequence of scalarized solutions for given λ and β.

Fig. 21 shows the constraints from Table 4 overlaid on top of the maximum scalar charge and the maximum black hole mass for scalarized black holes in the sGB theory with corresponding (β, λ) values. Only the constraints for two EOS have been displayed, namely WFF1 and MS1, that represent the two limiting cases considered in the previous subsection which lead to the strongest and the weakest constraint respectively.

7.3 Commentary

The results show that the more massive a pulsar is, the stronger the constraints which can be imposed from its observations on sGB gravity. In addition, these constraints are of course dependent on the nuclear matter EOS we employ but if we limit ourselves to modern realistic equations of state that are in agreement with the astrophysical observations, the spread is relatively small. Based on our results, though, and the present astrophysical observations related to the maximum neutron stars mass, one can conclude that the expected improvement can be up to a few tens of percent at most. One should keep in mind that these results are for sGB gravity with a massless scalar field. For a nonzero mass, the scalar charge will be zero and the scalar gravitational radiation will be suppressed similar to the DEF model thus leading to agreement with binary pulsar observations for more or less arbitrary theory parameters.

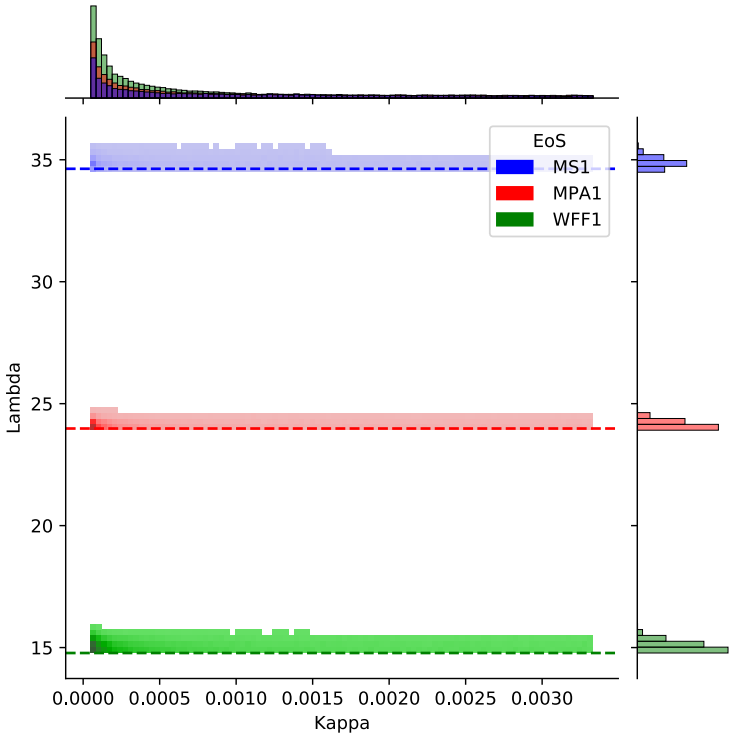

Figure 20: Comparison of the bifurcation point λ_{bif} (dashed line) and the MCMC samples scatter results for J0348+0432 with three realistic nuclear EOS. The colored region for each EOS is where scalarized neutron stars exist and their scalar radiation is within the observational bounds for the system. The region bellow the dashed line for each EOS has no constraints for the given NS–WD pair as it is bellow the bifurcation point, i.e. there scalarization for this pulsar mass is not possible and thus the scalar gravitational radiation is zero. Thus, even though this is also a region allowed by observation it has not been colored to avoid too many overlaps.

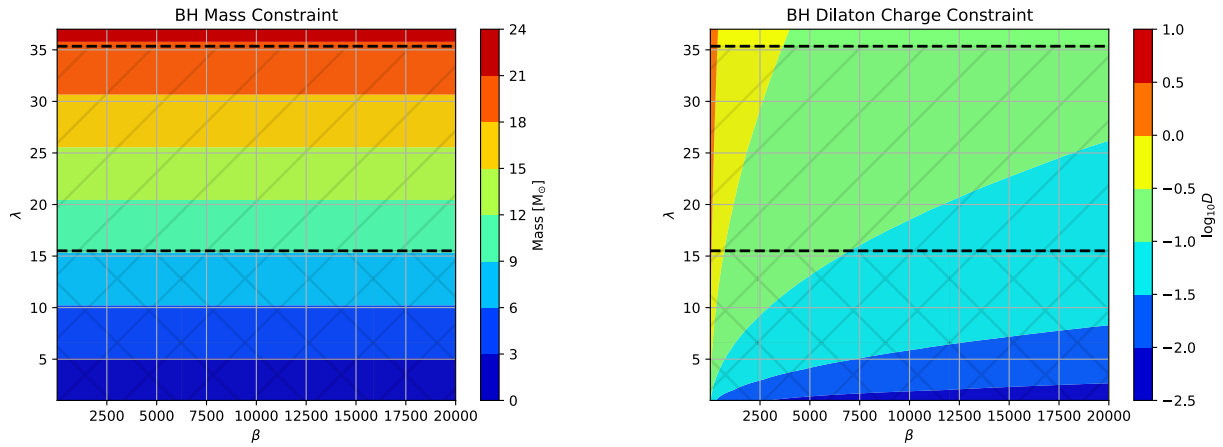

(a) Maximum BH mass in $M_\odot$

(b) Natural log of the maximum BH scalar charge

Figure 21: Comparison of the lowest and highest constraints arising from the J0348+0432 system based on the different EOS used with 95% one-sided quantile interval for λ. The shaded region with "x" pattern is where none of the EOSs provide any constraints on the parameters, i.e. scalarized neutron stars do not exist. The region marked with "/" is where at least one EOS provides some constraint on the parameters, i.e. scalarization exist for at least one of the considered EOS. The unmarked region is the one excluded from observations.

Having derived constraints on the sGB parameters λ and β, these have been transferred to static scalarized black holes in order to explore the possible range of astrophysically relevant solutions with scalar hair. The maximum mass of a static scalarized black hole has been obtained to be roughly $20M_\odot$ if a broad set of equations of state is considered, but this drops to approximately $9M_\odot$ for equations of state that are in the preferred range according to astrophysical observations such as NICER and the binary neutron star mergers. Thus, it turns out that it is not that easy to observe a scalarized black hole because of the fact that it should have a relatively small mass and only a limited number of such objects are expected to be observed in the near future. On the other hand, the maximum black hole scalar charge allowed by the binary pulsar observations is relatively large and can thus lead to observational signatures.

All of these results were obtained for one form of the coupling function that is quite generic. Based on the experience in other related problems, we believe that the constraints on the black hole properties will not change considerably even if we modify the coupling while still allowing for scalarization.

No constraints have been placed on the black holes for the case $\epsilon = -1$. The reason for that is that only rotating black holes can have scalar charge in this case in the so called spin-induced scalarization. Exploring this effect requires spinning black hole solutions in the sGB theory which introduces an additional free parameter – the angular velocity of the black hole, whick makes the constraints much more difficult to impose.

Thesis Contributions:

• Slowly rotating topological neutron stars were explored for the first time numerically. This class of compact objects in Tensor-Multi-Scalar Theories (TMST) were shown to obey standard polynomial universal relations between the mass, radius and the moment of inertia of the objects independently of the Equation of State (EOS). It was further shown that the values of the fit parameters are quite different not only between TMSTs and GR but also between compact objects with different topological charge in TMSTs. The exploration of the universal relation was carried out for two coupling functions of the scalar field – monotonic and non-monotonic. It was shown that in the case of the non-monotonic function, the solutions are restricted to a much smaller parameter space region and that their universal relations are virtually indistinguishable from GR. On the other hand, it was shown that for different topological charges of the non-monotonic coupling functions, deviations from GR independently of the EOS can be significant, exceeding 25% difference.

• Accretion-relevant quantities such as the innermost stable circular orbit (ISCO), orbital and epicyclic frequencies around topological neutron stars were computed numerically for the first time for different static and slowly-rotating configurations with the monotonic coupling function considered. It was shown that these do not differ significantly from GR and so X-ray observations of such objects are expected to be indisinguishable from observations of their equivalent in GR. Some quantitative observational traits in the case of a non-monotonic coupling function were commented from a theoretical point, which may produce observationally relevant traits of accretion discs around such objects after a more profound study.

• A novel class of universal relations for the mass, radius and central pressure/density/speed of sound at the maximum-mass point of a compact objects branch were shown to hold for scalarized neutron stars in STTs for the first time. It was shown that the fit parameters of these universal relations depend strongly on the theory and its parameters and that they can be used to pose constraints on equations of state (EOS) or theories based on observed or theoretically derived relations between the quantities involved. In addition, the universal relations both for GR and the STT were shown to hold also after adding non-baryonic equations of state using a total of 53 EOS for the fits. Even so, it was demonstrated that the addition of these non-baryonic EOS worsens the universality and increases the errors for the fits.

• Strong constrains on scalarization in scalar-Gauss-Bonnet (SGB) gravity were derived for the first time using observations of pulsars and white dwarfs in close binary systems. These constraints have been obtained for 12 different realistic equations of state and two different coupling functions through Bayesian inference. The likelihood function for that inference was formed from the difference between predicted and observed effects of gravitational waves emission and its effect on the orbits of these binary systems. In addition, the obtained constraints were used to impose the first strong constraints on scalarized black holes for one of the coupling functions which permits black holes to scalarize without high angular rates. As it turns out, these black holes cannot exceed roughly 10-20 solar masses depending on the exact equation of state, while their scalar charge can reach relatively high values.

Publications included in the thesis

Publications in international peer reviewed journals

• Danchev, V. I., Doneva, D. D. & Yazadjiev, S. S., Slowly rotating topological neutron stars: universal relations and epicyclic frequencies. Eur. Phys. J. C **80**, 878 (2020)

• Danchev, V. I. & Doneva, D. D., Constraining the equation of state in modified gravity via universal relations. Phys. Rev. D **103**, 024049 (2021)

• Danchev, V. I., Doneva, D. D. & Yazadjiev, S. S., Constraining scalarization in scalar-Gauss-Bonnet gravity through binary pulsars. Phys. Rev. D **106**, 124001 (2022)

Acknowledgements

I would like to thank my doctoral supervisor Prof. Stoycho Yazadjiev and my scientific consultant Dr. Daniela Doneva jointly for their dedication, support and mentorship over the course of my PhD. Separately, I would like to thank Prof. Yazadjiev for his theoretical insights and many lessons in analytical and mathematical apparatus even before I started my PhD, and I would like to thank Dr. Doneva for her insights into numerical methods and scientific computing which have unblocked my progress on many occasions.

I want to express my gratitude to all my colleagues at EnduroSat for their understanding and support during the past three years. I'd like to thank Raycho Raychev in particular for his advice and mentorship on many aspects of my professional development which are equally important in business, science and engineering.

I would like to thank my family for the patience and in particular my fiancee Zehra Abdrahim, for her understanding, continued support and many fruitful discussions throughout the years of my PhD studies. To my parents – thank you for igniting the spark of curiosity in me from a very early age!

I would also like to thank my former mentors and teachers who have made the most impact on my scientific development and growth apart from my doctoral supervisor: Petyo Nikolov, Nikola Karavasilev, Prof. Nikolay Vitanov, Dr. Hristo Dimov, Dr. Stoyan Pisov and Prof. Todor Mishonov.

I would like to give special thanks to those of my friends who are physicists and who contributed to my own understanding of physics through numerous discussions (in no particular order): Elton Shumka, Grigori Matein, Albert Varonov, Gospodin Karaivanov, Velizar Stoyanov, Ivan Tsonev, Chavdar Danchev and David Edwin Alvarez Castillo.

Last but not least, I would like to extend my thanks to Dr. S. Peter Worden who has greatly inspired me with our discussions and who continues to inspire me with his dedication and commitment to making humanity an interstellar species!

References

[1] Richard Baum and William Sheehan. *In search of planet Vulcan : the ghost in Newton's clockwork universe*. Plenum Trade, New York, USA, 1997.

[2] Thibault Damour and Gilles Esposito-Farese. Tensor multiscalar theories of gravitation. *Class. Quant. Grav.*, 9:2093–2176, 1992.

[3] M. Horbatsch, H. Silva, D. Gerosa, P. Pani, L. Gualtieri E. Berti, and U. Sperhake. Tensor-multi-scalar theories: relativistic stars and 3 + 1 decomposition. *Class. Quant. Grav.* ***32****, 204001*, 2015.

[4] Daniela D. D. Doneva and Stoytcho S. Yazadjiev. Topological neutron stars in tensor-multi-scalar theories of gravity. *Phys. Rev. D* ***101****, 064072*, 2020.

[5] P. Kanti, N. E. Mavromatos, J. Rizos, K. Tamvakis, and E. Winstanley. Dilatonic black holes in higher curvature string gravity. *Phys. Rev. D*, 54:5049–5058, 1996.

[6] K. S. Stelle. Renormalization of Higher Derivative Quantum Gravity. *Phys. Rev. D*, 16:953–969, 1977.

[7] Wolfgang Pauli. Über den zusammenhang des abschlusses der elektronengruppen im atom mit der komplexstruktur der spektren. *Zeitschrift für Physik*, 31:765–783, 1925.

[8] Jocelyn S. Read, Benjamin D. Lackey, Benjamin J. Owen, and John L. Friedman. Constraints on a phenomenologically parameterized neutron-star equation of state. *Phys. Rev. D*, 79:124032, 2009.

[9] J. R. Oppenheimer and G. M. Volkoff. On massive neutron cores. *Phys. Rev.*, 55:374–381, Feb 1939.

[10] Thomas Gold. Rotating neutron stars as the origin of the pulsating radio sources. *Nature*, 218:731–732, May 1968.

[11] Thomas Gold. Rotating neutron stars and the nature of pulsars. *Nature*, 221:25–27, Jan 1969.

[12] Jason W. T. Hessels, Scott M. Ransom, Ingrid H. Stairs, Paulo C. C. Freire, Victoria M. Kaspi, and Fernando Camilo. A radio pulsar spinning at 716 hz. *Science*, 311(5769):1901–1904, 2006.

[13] Hidemi Komatsu, Yoshiharu Eriguchi, and Izumi Hachisu. Rapidly rotating general relativistic stars - I. Numerical method and its application to uniformly rotating polytropes. *Monthly Notices of the Royal Astronomical Society*, 237(2):355–379, 03 1989.

[14] James B. Hartle. Slowly Rotating Relativistic Stars. I. Equations of Structure. *Astrophysical Journal*, 150:1005, Dec 1967.

[15] James B. Hartle. Slowly Rotating Relativistic Stars. II. Models for Neutron Stars and Supermassive Stars. *Astrophysical Journal*, 153:807, Sep 1968.

[16] James B. Hartle. Slowly rotating relativistic stars. *Astrophysics and Space Science*, 24:385–405, Oct 1973.

[17] M. Feroci and LOFT Consortium. The Large Observatory for X-ray Timing (LOFT). *Experimental Astronomy*, 34:415–444, Oct 2012.

[18] Robert Braun, T L Bourke, James A Green, Evan Keane, and Jeff Wagg. Advancing Astrophysics with the Square Kilometre Array. *PoS*, AASKA14:174, 2015.

[19] A. V. Bilous, A. L. Watts, A. K. Harding, T. E. Riley, Z. Arzoumanian, S. Bogdanov, K. C. Gendreau, P. S. Ray, S. Guillot, W. C. G. Ho, and D. Chakrabarty. A nicer view of psr j0030+0451: Evidence for a global-scale multipolar magnetic field. *The Astrophysical Journal Letters*, 887(1):L23, dec 2019.

[20] *Compact Stellar X-ray Sources*. Cambridge Astrophysics. Cambridge University Press, 2006.

[21] J. M. Lattimer and B. F. Schutz. Constraining the equation of state with moment of inertia measurements. *ApJ* ***629****, 979*, 2005.

[22] C. Breu and L. Rezzolla. Maximum mass, moment of inertia and compactness of relativistic stars. *MNRAS* ***459****, 646*, 2016.

[23] D. D. Doneva, S. S. Yazadjiev, and K. D. Kokkotas. I-q relations for rapidly rotating neutron stars in f(r) gravity. *Phys. Rev. D* ***92****, 064015*, 2015.

[24] Kalin V. Staykov, Daniela D. Doneva, and Stoytcho S. Yazadjiev. Moment-of-inertia–compactness universal relations in scalar-tensor theories and ∇^2 gravity. *Phys. Rev. D*, 93:084010, Apr 2016.

[25] Daniela D. Doneva Dimitar Popchev, Kalin V. Staykov and Stoytcho S. Yazadjiev. Moment of inertia-mass universal relations for neutron stars in scalar-tensor theory with self-interacting massive scalar field. *Eur. Phys. J. C* ***79****, 178*, 2019.

[26] D. D. Ofengeim. Universal properties of maximum-mass neutron stars: A new tool to explore superdense matter. *Phys. Rev. D*, 101:103029, May 2020.

[27] Kent Yagi and Nicolás Yunes. Approximate universal relations for neutron stars and quark stars. *Physics Reports*, 681:1–72, 2017. Approximate Universal Relations for Neutron Stars and Quark Stars.

[28] Eric Poisson and Clifford M. Will. *Gravity: Newtonian, Post-Newtonian, Relativistic*. Cambridge University Press, New York, USA, 2014.

[29] P. C. Peters. Gravitational Radiation and the Motion of Two Point Masses. *Phys. Rev.*, 136:B1224–B1232, 1964.

[30] Thibault Damour and Gilles Esposito-Farese. Tensor - scalar gravity and binary pulsar experiments. *Phys. Rev. D*, 54:1474–1491, 1996.

[31] Nicolás Yunes and Xavier Siemens. Gravitational-Wave Tests of General Relativity with Ground-Based Detectors and Pulsar Timing-Arrays. *Living Rev. Rel.*, 16:9, 2013.

[32] Brian C. Seymour and Kent Yagi. Testing General Relativity with Black Hole-Pulsar Binaries. *Phys. Rev. D*, 98(12):124007, 2018.

[33] Daniel Foreman-Mackey, David W. Hogg, Dustin Lang, and Jonathan Goodman. emcee: The MCMC Hammer. *Publ. Astron. Soc. Pac.*, 125:306–312, 2013.

[34] William H. Press, Saul A. Teukolsky, William T. Vetterling, and Brian P. Flannery. *Numerical Recipes: The Art of Scientific Computing*. Cambridge University Press, Cambridge, USA, third edition, 2007.

[35] J.R. Dormand and P.J. Prince. A family of embedded runge-kutta formulae. *Journal of Computational and Applied Mathematics*, 6(1):19–26, 1980.

[36] Donald W. Marquardt. An algorithm for least-squares estimation of nonlinear parameters. *Journal of the Society for Industrial and Applied Mathematics*, 11(2):431–441, 1963.

[37] Jonathan Goodman and Jonathan Weare. Ensemble samplers with affine invariance. *Communications in Applied Mathematics and Computational Science*, 5(1):65–80, January 2010.

[38] Daniela D. Doneva and Stoytcho S. Yazadjiev. Nontopological spontaneously scalarized neutron stars in tensor-multiscalar theories of gravity. *Phys. Rev. D* ***101****, 104010*, 2020.

[39] Victor I. Danchev, Daniela D. Doneva, and Stoytcho S. Yazadjiev. Slowly rotating topological neutron stars: universal relations and epicyclic frequencies. *Eur. Phys. J. C* ***80****, 878*, 2020.

[40] Lee Lindblom. Spectral representations of neutron-star equations of state. *Phys. Rev. D*, 82:103011, Nov 2010.

[41] Victor I. Danchev and Daniela D. Doneva. Constraining the equation of state in modified gravity via universal relations. *Phys. Rev. D*, 103:024049, Jan 2021.

[42] Thibault Damour and Gilles Esposito-Farèse. Nonperturbative strong-field effects in tensor-scalar theories of gravitation. *Phys. Rev. Lett.*, 70:2220–2223, Apr 1993.

[43] Compstar online supernovae equations of state. https://compose.obspm.fr. Accessed: 2022-12-24.

[44] N. K. Glendenning and S. A. Moszkowski. Reconciliation of neutron-star masses and binding of the Λ in hypernuclei. *Phys. Rev. Lett.*, 67:2414–2417, Oct 1991.

[45] Douchin, F. and Haensel, P. A unified equation of state of dense matter and neutron star structure. *A&A*, 380(1):151–167, 2001.

[46] M Oertel, C Providência, F Gulminelli, and Ad R Raduta. Hyperons in neutron star matter within relativistic mean-field models. *Journal of Physics G: Nuclear and Particle Physics*, 42(7):075202, jun 2015.

[47] A. Akmal, V. R. Pandharipande, and D. G. Ravenhall. Equation of state of nucleon matter and neutron star structure. *Phys. Rev. C*, 58:1804–1828, Sep 1998.

[48] H. Togashi, K. Nakazato, Y. Takehara, S. Yamamuro, H. Suzuki, and M. Takano. Nuclear equation of state for core-collapse supernova simulations with realistic nuclear forces. *Nuclear Physics A*, 961:78–105, 2017.

[49] Gordon Baym, Tetsuo Hatsuda, Toru Kojo, Philip D Powell, Yifan Song, and Tatsuyuki Takatsuka. From hadrons to quarks in neutron stars: a review. *Reports on Progress in Physics*, 81(5):056902, mar 2018.

[50] Gordon Baym, Shun Furusawa, Tetsuo Hatsuda, Toru Kojo, and Hajime Togashi. New neutron star equation of state with quark-hadron crossover. *The Astrophysical Journal*, 885(1):42, oct 2019.

[51] H.S. Köhler. Skyrme force and the mass formula. *Nuclear Physics A*, 258(2):301–316, 1976.

[52] B. K. Agrawal, S. Shlomo, and V. Kim Au. Nuclear matter incompressibility coefficient in relativistic and nonrelativistic microscopic models. *Phys. Rev. C*, 68:031304, Sep 2003.

[53] Paweł Danielewicz and Jenny Lee. Symmetry energy i: Semi-infinite matter. *Nuclear Physics A*, 818(1):36–96, 2009.

[54] L. Bennour, P-H. Heenen, P. Bonche, J. Dobaczewski, and H. Flocard. Charge distributions of ^{208}Pb, ^{206}Pb, and ^{205}Tl and the mean-field approximation. *Phys. Rev. C*, 40:2834–2839, Dec 1989.

[55] P.-G. Reinhard and H. Flocard. Nuclear effective forces and isotope shifts. *Nuclear Physics A*, 584(3):467–488, 1995.

[56] E. Chabanat. Ph.d. thesis: Interactions effectives pour des conditions extrêmes d'isospin. 1995.

[57] E. Chabanat, P. Bonche, P. Haensel, J. Meyer, and R. Schaeffer. A skyrme parametrization from subnuclear to neutron star densities. *Nuclear Physics A*, 627(4):710–746, 1997.

[58] E. Chabanat, P. Bonche, P. Haensel, J. Meyer, and R. Schaeffer. A skyrme parametrization from subnuclear to neutron star densities part ii. nuclei far from stabilities. *Nuclear Physics A*, 635(1):231–256, 1998.

[59] J. Friedrich and P.-G. Reinhard. Skyrme-force parametrization: Least-squares fit to nuclear ground-state properties. *Phys. Rev. C*, 33:335–351, Jan 1986.

[60] M. Baldo, I. Bombaci, and G. F. Burgio. Microscopic nuclear equation of state with three-body forces and neutron star structure. *Astronomy and Astrophysics*, 328:274–282, Dec 1997.

[61] Douchin, F. and Haensel, P. A unified equation of state of dense matter and neutron star structure. *A&A*, 380(1):151–167, 2001.

[62] T. Gaitanos, M. Di Toro, S. Typel, V. Baran, C. Fuchs, V. Greco, and H.H. Wolter. On the lorentz structure of the symmetry energy. *Nuclear Physics A*, 732:24–48, 2004.

[63] V. Dexheimer and S. Schramm. Proto-neutron and neutron stars in a chiral su(3) model. *The Astrophysical Journal*, 683(2):943, aug 2008.

[64] Bombaci, Ignazio and Logoteta, Domenico. Equation of state of dense nuclear matter and neutron star structure from nuclear chiral interactions. *A&A*, 609:A128, 2018.

[65] Hector O. Silva, Jeremy Sakstein, Leonardo Gualtieri, Thomas P. Sotiriou, and Emanuele Berti. Spontaneous scalarization of black holes and compact stars from a Gauss-Bonnet coupling. *Phys. Rev. Lett.*, 120(13):131104, 2018.

[66] Daniela D. Doneva and Stoytcho S. Yazadjiev. Neutron star solutions with curvature induced scalarization in the extended Gauss-Bonnet scalar-tensor theories. *JCAP*, 04:011, 2018.

[67] Rui Xu, Yong Gao, and Lijing Shao. Neutron stars in massive scalar-Gauss-Bonnet gravity: Spherical structure and time-independent perturbations. 11 2021.

[68] Lijing Shao, Noah Sennett, Alessandra Buonanno, Michael Kramer, and Norbert Wex. Constraining nonperturbative strong-field effects in scalar-tensor gravity by combining pulsar timing and laser-interferometer gravitational-wave detectors. *Phys. Rev. X*, 7(4):041025, 2017.

[69] Victor I. Danchev, Daniela D. Doneva, and Stoytcho S. Yazadjiev. Constraining scalarization in scalar-gauss-bonnet gravity through binary pulsars. *Phys. Rev. D*, 106:124001, Dec 2022.

[70] Daniela D. Doneva and Stoytcho S. Yazadjiev. New Gauss-Bonnet Black Holes with Curvature-Induced Scalarization in Extended Scalar-Tensor Theories. *Phys. Rev. Lett.*, 120(13):131103, 2018.

[71] Alexandru Dima, Enrico Barausse, Nicola Franchini, and Thomas P. Sotiriou. Spin-induced black hole spontaneous scalarization. *Phys. Rev. Lett.*, 125(23):231101, 2020.

[72] Daniela D. Doneva, Lucas G. Collodel, Christian J. Krüger, and Stoytcho S. Yazadjiev. Spin-induced scalarization of Kerr black holes with a massive scalar field. *Eur. Phys. J. C*, 80(12):1205, 2020.

[73] Daniela D. Doneva, Stella Kiorpelidi, Petya G. Nedkova, Eleftherios Papantonopoulos, and Stoytcho S. Yazadjiev. Charged Gauss-Bonnet black holes with curvature induced scalarization in the extended scalar-tensor theories. *Phys. Rev. D*, 98(10):104056, 2018.

[74] William E. East and Justin L. Ripley. Dynamics of Spontaneous Black Hole Scalarization and Mergers in Einstein-Scalar-Gauss-Bonnet Gravity. *Phys. Rev. Lett.*, 127(10):101102, 2021.

[75] John Antoniadis et al. A Massive Pulsar in a Compact Relativistic Binary. *Science*, 340:6131, 2013.

[76] K. Lazaridis et al. Generic tests of the existence of the gravitational dipole radiation and the variation of the gravitational constant. *Mon. Not. R. Astron. Soc.*, 400:805–814, 2009.

[77] Y. J. Guo1, P. C. C. Freire, et al. PSR J2222-0137. I. Improved physical parameters for the system. *A&A*, 654(A16):17, 2021.

[78] D. Mata Sánchez, A. G. Istrate, M. H. van Kerkwijk, R. P. Breton, and D. L. Kaplan. PSR J1012+5307: a millisecond pulsar with an extremely low-mass white dwarf companion. *Mon. Not. Roy. Astron. Soc.*, 494(3):4031–4042, 2020.

[79] Hao Ding, Adam T. Deller, Paulo Freire, David L. Kaplan, T. Joseph W. Lazio, Ryan Shannon, and Benjamin Stappers. Very long baseline astrometry of PSR J1012+5307 and its implications on alternative theories of gravity. *Astrophys. J.*, 896(1):85, 2020. [Erratum: Astrophys.J. 900, 89 (2020)].

[80] Paul J. McMillan. The mass distribution and gravitational potential of the Milky Way. *MNRAS*, 465:76–94, 2017.

[81] E. Fonseca et al. Refined mass and geometric measurements of the high-mass psr j0740+6620. *The Astrophysical Journal Letters*, 915(1), July 2021.

[82] Pulsar mass measurements and tests of general relativity. https://www3.mpifr-bonn.mpg.de/staff/pfreire/NS$_masses.html. Accessed$: $2021 - 12 - 28$.